

1 **Early mitochondrial stress and metabolic imbalance lead to photoreceptor cell death in**
2 **retinal degeneration**

3

4 Ke Jiang^{1*}, Anupam Kumar Mondal^{1*}, Yogita K. Adlakha^{1,2}, Jessica Gumerson¹, Angel Aponte³,
5 Linn Gieser¹, Jung-Woong Kim^{1,4}, Alexis Boleda^{1,5}, Matthew J. Brooks¹, Jacob Nellissery¹,
6 Donald A. Fox¹, Robert Balaban⁶, Raul Covian^{6§}, Anand Swaroop^{1§}

7

8 ¹Neurobiology, Neurodegeneration & Repair Laboratory, National Eye Institute, National Institutes
9 of Health, Bethesda, Maryland, USA,

10 ²Translational Health Science and Technology Institute, National Capital Region Biotech Cluster,
11 Faridabad, India,

12 ³Proteomics Core Facility, National Heart, Lung and Blood Institute, National Institutes of Health,
13 Bethesda, Maryland, USA

14 ⁴Department of Life Science, College of Natural Sciences, Chung-Ang University, Seoul 156-756,
15 Republic of Korea,

16 ⁵Center for Bioinformatics and Computational Biology, University of Maryland, College Park,
17 Maryland, USA,

18 ⁶Laboratory of Cardiac Energetics, National Heart, Lung, and Blood Institute, National Institutes of
19 Health, Bethesda, Maryland, USA.

20

21 * Equal contribution

22 § Co-corresponding authors

23

24 Lead contact: Anand Swaroop, Ph.D., Neurobiology-Neurodegeneration & Repair Laboratory,
25 National Eye Institute, National Institutes of Health, MSC0610, 6 Center Drive, Bethesda, MD, USA.

26 Phone: 301.435.5754; Fax: 301.480.9917; E-mail: swaroopa@nei.nih.gov

27

28 **ABSTRACT**

29 Neurodegenerative diseases exhibit extensive genetic heterogeneity and complex etiology with
30 varying onset and severity. To deduce the mechanism leading to retinal degeneration, we
31 adopted a temporal multi-omics approach and examined molecular and cellular events before
32 the onset of photoreceptor cell death in the widely-used *Pde6b^{rd1/rd1}* (*rd1*) mouse model.
33 Transcriptome profiling of neonatal and developing rods revealed early downregulation of genes
34 associated with anabolic pathways and energy metabolism. Quantitative proteomics of *rd1*
35 retina showed early changes in calcium signaling and oxidative phosphorylation, with specific
36 partial bypass of complex I electron transfer, which precede the onset of cell death.
37 Concurrently, we detected alterations in central carbon metabolism, including dysregulation of
38 components associated with glycolysis, pentose phosphate and purine biosynthesis. *Ex vivo*
39 assays of oxygen consumption and transmission electron microscopy validated early and
40 progressive mitochondrial stress and abnormalities in mitochondrial structure and function of *rd1*
41 rods. These data uncover mitochondrial over-activation and related metabolic alterations as
42 early determinants of pathology and implicate dysregulation of calcium signaling as the initiator
43 of higher mitochondrial stress, which then transitions to mitochondrial damage and
44 photoreceptor cell death in retinal degeneration. Our studies support the “one hit model” arguing
45 against the cumulative damage hypothesis but suggest that cell death in neurodegenerative
46 disease is initiated by specific rather than a random event.

47

48 **KEYWORDS**

49 Retinal degeneration, Vision, Phototransduction, *rd1*, Mitochondria, Metabolome, Proteome,
50 Transcriptome, Complex I, Oxidative phosphorylation, Energy homeostasis, Central carbon
51 metabolism, Calcium signaling

52 INTRODUCTION

53 Neurodegenerative diseases are characterized by progressive dysfunction and death of post-
54 mitotic neuronal cells that lead to severe cognitive and/or sensory defects, greatly impacting the
55 quality of life. These largely untreatable pathologies typically afflict specific neurons, with
56 divergent clinical manifestations caused by heterogenous genetic factors ^{1,2}. Genes and
57 pathways implicated in neurodegeneration participate in energy metabolism, signaling, stress
58 response, and autophagy, among other homeostatic processes ³⁻⁵. Mitochondrial dysfunction is
59 arguably a key factor in neurodegenerative disease ⁶⁻⁸. However, the concept of increased
60 stress of functional mitochondria ⁹ has been largely underappreciated. One carbon and serine
61 metabolism pathways are also implicated in health and pathology and may provide novel
62 therapeutic targets ^{10,11}. To date, we still lack knowledge of the precise cellular events,
63 especially integrative molecular cues convergent at the onset of pathology that determine the
64 natural history of neuronal cell death in degenerative disease.

65 The retina, the most accessible part of the central nervous system, provides an excellent
66 model for examining neurodegeneration. Retinal and macular degenerative diseases constitute
67 a major cause of incurable vision impairment worldwide, with pathogenic mutations identified in
68 almost 300 genes (<https://sph.uth.edu/retnet/>). Extensive genetic and phenotypic heterogeneity
69 associated with Mendelian retinal diseases ^{12,13} make the design of gene-based therapies
70 particularly challenging ^{14,15}. The death of photoreceptor cells, predominantly by apoptosis, is
71 the primary end-point that leads to vision loss in most retinal diseases ^{16,17}, and thus anti-
72 apoptotic interventions have been attempted to restore vision ¹⁸. The “one-hit model” of cell
73 death in neurodegeneration argues against the cumulative damage hypothesis and suggests
74 that mutations create an adaptive state of equilibrium and cell death is initiated by single
75 random event ¹⁹. We and others hypothesized convergence in pathways leading to pathology in
76 divergent inherited retinal diseases ^{20,21}. The prodromal events and critical mutant steady state
77 preceding photoreceptor cell death are poorly understood.

78 Spontaneous and transgenic mouse mutants can elegantly phenocopy human retinal
79 disease^{22,23}; albeit, the onset and severity may vary. We chose a widely-studied retinal
80 neurodegeneration model, the retinal degeneration 1 mouse (*rd1*; also referred as *Pde6b*^{*rd1/rd1*}),
81 to investigate early molecular and cellular events that may trigger photoreceptor cell death. The
82 *rd1* mouse is homozygous for the loss of function genetic defect in the *Pde6b* gene, which
83 encodes the rod photoreceptor-specific cGMP phosphodiesterase 6 β subunit (PDE6 β)^{24,25}.
84 PDE6 β is an evolutionarily conserved key component which is localized in rod outer and inner
85 segments²⁶ and mediates phototransduction by controlling cGMP levels and facilitating the
86 opening of cGMP-gated ion channels²⁷. The rod cell death in *rd1* mouse retina is histologically
87 evident starting at postnatal day (P)10, with a complete loss of the photoreceptor outer nuclear
88 layer (ONL: composed of rod and cone nuclei) by P30. Mutations in the human *PDE6B* gene
89 lead to a spectrum of autosomal recessive retinal degeneration phenotypes²⁸.

90 Here, we report widespread prodromal pathophysiological changes in the neonatal *rd1*
91 retina using an integrative multi-omics approach that included temporal transcriptomics of
92 purified rod photoreceptors along with proteomic and metabolomic analysis of whole retinas in
93 combination with structural and functional assays. These data demonstrate a higher
94 mitochondrial stress as early as P6; much before photoreceptor cell death is evident in the
95 mutant retina. We show, for the first time, that calcium signaling defects which drive
96 mitochondrial and metabolic alterations constitute the pre-death mutant state in rod
97 photoreceptors. These results are consistent with the known high metabolic demand and activity
98 of photoreceptors²⁹⁻³¹. Our findings of prodromal molecular and functional dysfunction in
99 mitochondria and their associated cell signaling regulation are the earliest detected etiology of
100 rod cell death and support the proposed convergence of cellular events during retinal
101 neurodegeneration^{2,20,21}.

102

103 **RESULTS**

104 **Early transcriptomic divergence in the *rd1* rods reveals altered metabolic and signaling**
105 **pathways**

106 Gross morphological changes and cell death markers are detected in rod photoreceptors of *rd1*
107 mouse retina starting at or around P10, and early pathology is characterized by shorter outer
108 segments and progressive thinning of the ONL (Figure 1A). Since the genetic and biochemical
109 defect is limited to these retinal cells, we first performed transcriptome profiling of newborn and
110 developing rod photoreceptors. We generated *rd1*-GFP mice by mating the *Pde6b*^{*rd1/rd1*} mice to
111 *TgNrlp-EGFP* (*WT*)³² mice, used flow cytometry to purify GFP⁺ rods at P2, P4, P6, P8 and P10
112 (before rod cell death is evident), and performed RNA-seq analysis (Figure 1A). After rigorous
113 filtering and normalization, we captured expression of 14,534 genes from temporal
114 transcriptome profiles of *rd1* and *WT* photoreceptors. Principal component analysis (PCA) of *rd1*
115 and *WT* samples showed progressively divergent RNA profiles as early as P2 (the peak of rod
116 birth is P0-P2), the earliest time we sampled the purified rods (Figures 1B and 1C). Heat maps
117 of a total of 1,474 differentially expressed genes (DEGs) displayed distinct patterns (shown as
118 clusters C1-C10: see below) in *rd1* rods at pre-degeneration states (Figure 1D).

119 KEGG pathway enrichment analysis of DEGs revealed that central carbon metabolism
120 and signaling pathways were prominently impacted in the early stages of developing *rd1* rods
121 (Figures 1E, S1 and S2). Metabolism related DEGs at P2, P4 and P6 included those associated
122 with carbohydrate metabolism, cellular anabolic processes, and fatty acid biosynthesis (Figures
123 1E, S1A-S1C and S2) and corresponded primarily to glycolysis (e.g., *Pfkfb2*, *Tigarr*, and *Pfkfb2*),
124 oxidative phosphorylation (OXPHOS; e.g., *Ndufs2*, *Atp5o* and *mt-Nd3*), pentose phosphate
125 pathway (PPP) (e.g., *H6pd*), purine metabolism (e.g., *Pnp*), and glycogenolysis (e.g., *Ag1* and
126 *Pgm1*) (Figures 1E, S1B and S2). A number of lipid metabolism genes exhibited higher
127 expression; e.g., fatty acid biosynthesis gene *Acot1* and several phospholipid metabolism genes
128 (*Abhd4*, *Lpcat2*, and *Samd8*) (Figures S1B and S2). Additionally, homocysteine and one carbon

129 metabolism genes – *Ahcy*, *Mthfr* and *Mthfd2* – were among those showing the highest fold
130 change differences (Figure S1B, Table SData1). The gene coding for myoferlin (*Myof*) was
131 markedly under-expressed in *rd1* rods (Figure S1B), even though its consequence in neuronal
132 cells remains unspecified. Transcriptional modulators, such as *Duxbl1*, *Sox30* and *Hmga1b*, and
133 mitochondrial stress regulator *Atf4* were also significantly differentially expressed in the early
134 developing rods (Figure S2). Importantly, we observed differential expression of calcium-related
135 signaling genes (e.g., *Hcn*, *S100a10*, *Atf4*) in *rd1* rods at early stages, much before the onset of
136 degeneration at P10 (Figures S1C and S2). Finally, genes involved in the phototransduction
137 pathway demonstrated significantly altered expression at these early ages (Figure S1A).

138 *Rd1* rod DEGs could be grouped into 10 clusters (C1-C10). Three of the larger clusters
139 showed concordance with changes in distinct pathways (Figures 1D, S1D and S1E). Cluster 1
140 (C1) genes consistently demonstrated higher expression in *rd1* rods starting at P2 and included
141 metabolic genes for one carbon pool, purine metabolism, and fatty acid metabolism.
142 Conversely, genes in C3 cluster with low expression in *rd1* rods belonged to phototransduction
143 and hedgehog signaling. Cluster C2 showed sharp induction of gene expression at the onset of
144 degeneration (P10) and contained fatty acid biosynthesis, ferroptosis as well as
145 phototransduction genes.

146

147 **Reduced expression of mitochondrial NADH dehydrogenase complex and signaling** 148 **proteins in *rd1* retina**

149 In developing mouse retina, the photoreceptor differentiation is concordant with major changes
150 in the transcriptome between P6 and P10³³. We therefore wanted to ascertain whether disease-
151 specific trends in *rd1* gene expression further translate to proteome changes that precede
152 developmental milestones and onset of degeneration. Mass spectrometry-based proteome
153 analysis of P6 and P10 *rd1* and *WT* retina identified a total of 4,955 proteins. Of these, 621 were
154 differentially expressed in P6 *rd1* retina and an additional 630 showed altered expression at P10

155 (Figures 2A and S3A). Gene set enrichment analysis (GSEA) using Fast Gene Set Enrichment
156 Analysis (*fgsea*) uncovered mitochondrial electron transport chain (ETC) as the most
157 downregulated pathway in both P6 and P10 *rd1* retina (Figures 2B and S3B) with specific
158 reductions in the subunits of NADH dehydrogenase (complex I) (Figure 2C). Further targeted
159 analysis, using a curated GSEA, confirmed a significant negative enrichment of the OXPHOS
160 pathway at P6 and P10 (Figure S3C). This trend begins a negative course at P6 with further
161 reductions by P10, clearly showing a correlation of OXPHOS impairment with age in *rd1* retina.
162 Leading-edge analysis identified complex I subunits to be the driver of OXPHOS impairment,
163 with other ETC complexes showing insignificant changes (Figure 2D). Complex I enzymatic
164 activity assay in mitochondria-enriched retinal extracts also showed lower activity in *rd1* retina
165 between P2 and P8 (Figure S3D), confirming an impairment of complex I function.

166 Manual curation of significantly altered mitochondrial proteins uncovered over-
167 expression of several ribosomal proteins, tRNA ligases, import/processing subunits and
168 ubiquinone biosynthesis proteins at P6 and P10, suggesting a more active mitochondrial
169 biogenesis in *rd1* retina (Figure 3A). For example, the most over-expressed mitochondrial
170 protein (SUPV3L1, $FC_{P6} = 4.98$) is an RNA helicase associated with the RNA surveillance
171 system in mitochondria³⁴, suggesting enhanced transcription of mitochondrial DNA. In addition,
172 several proteins involved in assembly of respiratory complexes were increased in *rd1* retina
173 (ATPAF1, TTC19, AIFM1 and NLN). Furthermore, increased expression of amino acid
174 degradation enzymes (GLDC, IVD, MCCC2) suggested an augmented degradation of
175 mitochondria in *rd1* retina, resulting in a faster mitochondrial turnover due to a parallel increase
176 in biogenesis. In addition, mitochondria in the mutant retina seem to exhibit a higher capacity to
177 donate electrons directly into the ubiquinone pool bypassing complex I, as suggested by higher
178 expression of enzymes involved in fatty acid oxidation (MCEE, ECI2, HADHA, ECH1, ECI1),
179 leucine degradation (IVD, MCCC2) and pyrimidine metabolism (DHODH).

180 Curiously, a similar analysis of the strategically upstream glycolytic, PPP and TCA cycle
181 proteins did not show a pathway-wide consistent difference, although a few specific proteins
182 including PFKP, SLC16A3, HK2, PDK1 and PDK2 were significantly different at one or both
183 ages (Figure 3B). Consistent with the significant under-expression of the pyruvate
184 dehydrogenase kinase PDK2 at P6 and P10, we observed reduction in ratios of single- and
185 double-phosphorylated peptides from subunit E1 α of the pyruvate dehydrogenase complex
186 (PDC) in *rd1* at both P6 and P10 (Figure 3C). When analyzing the differential protein expression
187 of all calcium-associated proteins, robust and consistent calcium dysregulation was evident in
188 the *rd1* retina (Figure 3D). One of the most downregulated proteins in the *rd1* retina was
189 calmodulin (CALM1) (Figure S3A), which serves as the primary intracellular calcium sensor and
190 initiator of downstream signaling events that correspond to changing calcium levels. In addition,
191 calcium-binding mitochondrial carrier proteins, such as SLC25A13 (fold change at P6, $FC_{P6} =$
192 1.48) and SLC25A25 ($FC_{P6} = 0.43$), were significantly altered. Interestingly, the highest
193 overexpressed protein in *rd1* retina was PITPNM3 ($FC_{P6} = 2.63$), a membrane-associated
194 phosphatidylinositol transfer protein implicated in autosomal dominant cone rod dystrophy³⁵.
195 These findings strongly indicate abnormal calcium signaling in the *rd1* retina at early stages
196 before the onset of degeneration.

197

198 **Metabolite imbalance especially of central carbon pathways in *rd1* retina**

199 To further dissect early stages of neurodegeneration, we examined 116 metabolites in *rd1* and
200 *WT* retina at P6 (Figure 4) and P10 (Figure S4). We detected alterations in glycolytic and PPP
201 intermediates as well as nucleotides at both stages (Figures 4A and S4A). Carnosine, a
202 dipeptide involved in resistance to oxidative stress and divalent ion chelation³⁶ was the most
203 elevated metabolite in the P6 *rd1* retina. We generated a metabolite-pathway network and
204 identified biosynthesis of amino acids, carbon metabolism, ATP-binding-cassette transporters,
205 purine metabolism and PPP as those with the most difference in metabolites (Figure 4B).

206 We then focused on central carbon metabolism (i.e., glycolysis, PPP and purine
207 metabolism) because of significant aberrations in the P6 *rd1* retina. We observed a significant
208 decrease in the upstream intermediates (glucose 6-phosphate, fructose 6-phosphate, fructose
209 1,6-biphosphate and dihydroxyacetone phosphate) (Figure 4C), yet downstream glycolytic
210 intermediates and products such as glycerol 3-P and glycerol (required for phospholipid
211 synthesis) as well as pyruvate and lactate were relatively unchanged. Together, these data
212 suggest that the net glycolytic flux did not decrease at this early stage (i.e., by P6). Our results
213 also demonstrated significant depletion of most PPP intermediates in the *rd1* retina. In contrast,
214 we observed a marked increase of purine triphosphates and their respective nucleobases,
215 apparently at the expense of early purine biosynthesis intermediates including adenosine and
216 guanosine and their monophosphorylated forms (Figure 4D). Thus, significant reductions of total
217 metabolite concentrations in glycolysis and PPP were observed in the *rd1* retina as early as P6
218 and even at P10 (Figures 4E and S4B). These metabolic changes suggest a shift in carbon
219 utilization rather than a decrease in metabolic flux through these pathways.

220

221 **Pre-degeneration functional and morphological defects in *rd1* mitochondria**

222 Higher ATP concentrations in P6 *rd1* retina (see Figure 4D) suggested higher OXPHOS activity.
223 To directly assess mitochondrial respiration coupled to ATP production in relation to maximal
224 (uncoupled) respiratory activity, we measured oxygen consumption rate (OCR) in acutely
225 isolated, *ex vivo* retinal punches from *rd1* and *WT* mice (Figure 5A) using a previously optimized
226 protocol⁹. We noted that basal mitochondrial OCR (coupled to ATP production) decreased in
227 *WT* retina during development, reaching a low point at P10, followed by an increase at eye
228 opening on P14 (Figure 5B). In contrast, the *rd1* retinas showed a trend of higher basal OCR
229 compared to *WT* as early as P3 (Figure 5B). With the onset of degeneration after P10 (see
230 Figure 1A), basal mitochondrial OCR in *rd1* retina was reduced significantly at P14 (Figure 5B)
231 when as many as 50% of the rod photoreceptors are lost. After adding a mitochondrial

232 uncoupler (Bam15) to obtain the maximal OCR, the mitochondrial reserve capacity (MRC) was
233 obtained by calculating the additional percentage of maximal OCR that is not used for ATP
234 production under basal conditions. In developing *WT* retina, MRC progressively increased and
235 peaked to ~50% around P8 and P10 before decreasing to ~30% at P14 (Figure 5B), consistent
236 with our previous observations of low MRC in healthy adult retina⁹. Interestingly, *rd1* retinas
237 were characterized by lower MRC values from P3 through P10 before overt rod degeneration
238 was observed at P14. MRC was markedly increased at P14 by 50-60%, as previously reported⁹
239 (Figure 5B).

240 To assess whether enhanced oxygen consumption might result from increased number
241 of mitochondria in the *rd1* retina, we examined the Mit/Nu DNA ratio³⁷. Quantitative qPCR
242 analysis demonstrated a trend of lower Mit/Nu DNA ratios in *rd1* retina, suggesting relatively
243 fewer mitochondria in P2 to P8 *rd1* retina compared to age-matched *WT* retina (Figure S5).

244 Ultrastructural analysis by transmission electron microscopy (TEM) revealed delayed
245 organization of the rod inner segments and morphological defects in mitochondria cristae
246 structure as early as P6 in the *rd1* retina (Figure 6). At P8, abnormal mitochondria were more
247 prevalent in inner segments of *rd1* rod photoreceptors and showed loss of inner membrane
248 cristae and a swollen vesicular appearance. However, a majority of mitochondria at this stage
249 still exhibited normal gross morphology. Swollen mitochondria were larger and more numerous
250 in *rd1* rods at P10, indicating a disrupted mitochondrial network even before the histological rod
251 cell death was observed. With extensive degeneration evident at P14, few mitochondria in *rd1*
252 rods had a normal gross or ultrastructural morphology, and the retina exhibited a disrupted
253 overall structure and lamination (Figure S6).

254

255 **Proposed model of molecular and cellular events leading to photoreceptor cell death**

256 Temporal dynamics of transcriptome changes, together with proteomic and energy metabolism
257 defects detected at early stages in the *rd1* retina, enabled us to construct a model to explain the

258 etiology of rod photoreceptor cell death in the *rd1* mouse (Figure 7). Important features
259 identified in our study include progressively increasing metabolic alterations and mitochondrial
260 deficiencies that were initiated prior to any observed morphological and/or functional defects in
261 degenerating rod photoreceptors of the *rd1* mouse. We hypothesize that a functional imbalance
262 in pathways associated with one-carbon metabolism and energy homeostasis, as indicated by
263 RNA profiles of newborn rod photoreceptors, results in down regulation of complex I, and
264 aberrant mitochondrial structure and function. As a consequence of reduced electron flow
265 through the ETC from NADH oxidation, the ubiquinone pool receives more electrons from other
266 sources such as fatty acid oxidation, as well as glycine, leucine and valine metabolism.
267 Concurrently, expression levels of a key intracellular calcium regulator, calmodulin, are greatly
268 reduced leading to dysregulation of mitochondrial calcium uptake and calcium-dependent
269 signaling pathways (e.g., the activation of PDC through calcium-activated dephosphorylation by
270 PDP). Activated PDC draws from the pyruvate pool and can enhance the flux through glycolysis
271 pathway. A decrease in upstream metabolites of both glycolysis and PPP supports this
272 hypothesis. Furthermore, disease-related activity of the one-carbon cycle and homocysteine
273 metabolism can aggravate cellular distress by potentially altering NADPH levels, consistent with
274 observed differences in purine metabolism. In parallel, later accumulation of cGMP in *rd1*
275 mutants may also lead to differential abundance of purine molecules, reflecting the rod cell's
276 attempts to control purine production by metabolic reorganization, which can further contribute
277 to initiation of molecular pathology. Thus, an increasing and accumulating imbalance of energy
278 metabolism pathways coupled with a progressive increase in intracellular and mitochondrial
279 calcium levels result in elevated mitochondria stress and calcium overload, eventually leading to
280 mitochondria swelling and rod photoreceptor cell death in the *rd1* retina.

281

282 **DISCUSSION**

283 The lack of regenerative potential in the mammalian retina makes photoreceptor cell dysfunction
284 and/or death a leading cause of incurable blindness. Rod photoreceptors are specifically
285 vulnerable to degeneration, and their deficiency is generally followed by the loss of cones in
286 inherited retinal diseases²¹. Even in a multifactorial disorder affecting the macula (namely age-
287 related macular degeneration, AMD), rod cell death precedes cone loss³⁸. Convergence to rod
288 degeneration despite extensive clinical and genetic heterogeneity suggests commonalities in
289 molecular and cellular pathways and offers opportunities for gene-agnostic intervention in retinal
290 and macular diseases^{20,21}. As an example, a thioredoxin-like protein RdCVF has been shown to
291 protect cone function in multiple distinct models of retinal degeneration by inducing glucose
292 uptake and aerobic glycolysis³⁹. We hypothesized that the presence of a genetic mutation
293 would exert specific impact(s) on molecular/biochemical pathways in target cells early in
294 development and that progressive and varying deterioration of cellular responses would
295 eventually lead to cell death²⁰. By applying three ‘omics’ technologies, here we demonstrate
296 that the loss of PDE6 β by an inherited mutation results in extensive adaptations in metabolic
297 and mitochondrial components of newborn and developing rod photoreceptors, much before the
298 established critical requirement of PDE6 β in signaling during phototransduction. Our studies
299 identify early convergence of multiple cellular responses to mitochondria-related metabolic and
300 signaling pathways and point to disruptions or reallocations of energy resources and calcium
301 signaling in early stages preceding the onset of retinal neurodegeneration.

302 The *rd1* mouse represents arguably the most studied model of retinal degeneration.
303 PDE6 β is associated with controlling cGMP levels, and cGMP accumulation has been
304 implicated in driving the death of rod photoreceptors in the *rd1* retina as well as in
305 phototransduction-associated inherited retinal diseases^{17,40,41}. cGMP is a key second
306 messenger in multiple cellular signaling pathways. In photoreceptors, cGMP-gated channels
307 control the flux of ions in light and dark conditions contributing to Ca²⁺ homeostasis⁴².

308 Remarkably however, photoreceptor cell death begins in *rd1* retina around P10 and before eye
309 opening in mouse (at P14). Whilst most studies focused on the disease progression at or after
310 onset of rod death (after P10), our transcriptome profiling of neonatal (P2-P6) *rd1* rods shows
311 major and highly specific abnormalities in expression of genes associated with central carbon
312 metabolism. These early changes likely impact energy homeostasis, redistribute metabolites
313 within one-carbon pathways, and initiate a cascade of signaling events. Two of the earliest
314 differentially expressed genes – *Ahcy* (lower expression) and *Mthfr* (high expression) –
315 regulating the one-carbon metabolism are significantly altered with high magnitude and
316 influence nucleic acid synthesis and the balance of S-adenosylmethionine to S-
317 adenosylhomocysteine (SAM/SAH) ratio. Continued differential expression of *Ahcy* and *Mthfr* is
318 reflected by an increase in SAM in the metabolome data from P10 *rd1* retina, suggesting a shift
319 in pan-methylation status. The differential gene expression trends suggest that mutant
320 photoreceptors never undergo normal development despite their normal morphological
321 appearance in early stages. Proteomic and metabolomic data from P6 *rd1* retina further
322 supports these findings and implicates mitochondria and related metabolic and calcium
323 signaling pathways as the early mediators of the cellular response in retinal neurodegeneration.

324 Photoreceptors have high energy requirements for maintaining their physiological state
325 in dark and light⁴³. Like other neurons, glucose provides the primary source of energy in
326 photoreceptors^{9,44}, and the stimulation of glucose uptake and/or metabolic intermediates can be
327 neuroprotective in photoreceptor degeneration^{39,45-47}. Specialized cristae architecture, low
328 reserve capacity and high OXPHOS of mitochondria^{9,44,48} validate their primary role in providing
329 the energy requirements of photoreceptors. Distinctive reduction in complex I subunits and
330 alterations in several mitochondrial proteins (including others associated with ETC complexes)
331 in P6 *rd1* retina strongly argue in favor of altered mitochondrial structure and function being
332 early indicators of photoreceptor stress. Predictably, we detected lower complex I activity in *rd1*
333 retina, consistent with a previous report⁴⁹. However, a partial deficiency in complex I activity

334 can be compensated by alternate pathways that donate electrons at the level of the ubiquinone
335 pool. Several of these pathways are augmented in *rd1* retina as indicated by increase in
336 proteins associated with fatty acid oxidation (MCEE, ECI2, HADHA, ECH1, ECI1), leucine
337 degradation (IVD, MCCC2) and pyrimidine metabolism (DHODH). These results of partial
338 bypassing of complex I electron transfer are in accordance with the higher basal mitochondrial
339 OCR used for ATP production and enhanced ATP content.

340 As an indicative parameter of mitochondrial health/stress, the MRC can be affected by
341 several factors, including the ability of the cell to deliver substrate(s) to mitochondria and
342 functional capacity of enzymes involved in electron transport⁵⁰. Reduced MRC in *rd1* retina as
343 early as P3 suggests that a fraction of mitochondria in mutant photoreceptor cells have
344 undergone uncoupling, as reported in cells during injury and aging as an adaptive response to
345 decrease reactive oxygen species (ROS)⁵¹. Changes in MRC are also correlated with oxidative
346 stress, calcium overload and cone cell death⁵². A lower MRC and higher OCR in the *rd1* retina
347 are consistent with chronically higher calcium concentrations in photoreceptors, as reported as
348 early as P5⁵³, which would at first stimulate OXPHOS⁵⁴ and ATP production but then cause
349 swelling and mitochondrial damage by increasing ROS formation and inner membrane
350 depolarization. Moreover, a faster flow of electrons to the ubiquinone pool to compensate for
351 partial complex I deficiency may also result in enhanced ROS. Our ultrastructural observations
352 show progressive mitochondrial damage in developing *rd1* rods. The higher content of proteins
353 involved in biogenesis and degradation suggests a faster turnover to regenerate functional
354 mitochondria. The observed lower Mit/Nu DNA ratios in *rd1* retina supported this hypothesis.
355 With progressive calcium overload, mitochondrial respiration is inhibited and accompanied by
356 cytochrome c release, decreased ATP production and disruption of the mitochondrial matrix and
357 cristae⁵⁵.

358 High aerobic glycolysis is a characteristic feature of photoreceptor cells and crucial for
359 anabolic demands and functional homeostasis^{30,56}. In our study, glycolytic abnormalities in pre-

360 degeneration stage *rd1* photoreceptors are noted by significant over-expression of two
361 important regulators: *Tigar* and *Pfkfb2*. TIGAR is a negative regulator of glycolysis, whereas
362 PFKFB2 modulates the pathway by controlling the pool of fructose-2,6-bisphosphate ⁵⁷. Though
363 we did not detect significant change in pyruvate, lactate or acetyl-CoA, the evidence from
364 proteomic profiling indicates re-programming of the Tricarboxylic Acid (TCA) cycle in the *rd1*
365 photoreceptors. Mitochondrial PDC links glycolysis and the TCA cycle, modulating the overall
366 rate of oxidation of carbohydrate fuels under aerobic conditions ⁵⁸. Significantly lower content of
367 one isoform of PDC kinase (PDK2) and reduced phosphorylation of the PDC E1 alpha subunit
368 in P6 and P10 *rd1* retina suggest a faster-working PDC, which can potentially accelerate flux
369 through the TCA cycle. Our data are concordant with previously reported prolonged
370 photoreceptor survival in mouse models of retinal degeneration by increasing glycolysis flux
371 through inhibition of SIRT6 ⁴⁶ or by promoting lactate catabolism as fuel by Txnip administration
372 ⁴⁷. We propose that the faster PDC activity, besides being the consequence of higher
373 mitochondrial calcium, could be an adaptive response of mutant photoreceptors by fine tuning
374 TCA cycle in dealing with the stress. A recent report demonstrating slowdown of disease
375 progression in *Pde6α* and *Rho*^{P23H} mouse models by dietary supplementation of TCA cycle
376 intermediates, α -ketoglutarate and citrate, also supports our hypothesis ⁵⁹.

377 Elevated intracellular calcium cannot be explained by PDE6 β 's role in phototransduction
378 at early stages before eye opening. Notably, our metabolomic data does not reveal a significant
379 difference in cGMP concentration between P6 or P10 *WT* and *rd1* retina, even though
380 mitochondrial structural defects were observed as early as P6 and P8. Interestingly, calmodulin,
381 a key regulator of numerous calcium-sensitive proteins, is nearly undetectable at P6 in the *rd1*
382 retina, suggesting a dysregulation of calcium-dependent signaling at an early stage. Given that
383 calmodulin directly interacts with PDE ⁶⁰, we propose that the loss of PDE6 β compromises
384 calmodulin stability or activity, and in turn, affects other calcium-dependent processes. Indeed,

385 our proteomic data reveals altered expression of a number of calcium-regulated proteins in the
386 *rd1* retina. Furthermore, calmodulin controls the sensitivity of rod cGMP channels to cGMP in a
387 calcium-dependent manner, and with a decrease in calmodulin, cGMP channels exhibit a higher
388 affinity for cGMP and more readily open to allow the influx of calcium into the inner segments⁶¹.
389 This is a more feasible explanation for the initiation of calcium-mediated mitochondria injury that
390 we detect as early as P6. The absence of PDE6 β activity during phototransduction likely
391 amplifies the damage at eye opening (P14), resulting in rapid photoreceptor loss in the *rd1*
392 retina.

393 Our studies argue against the cumulative damage and support an adaptive mutant state
394 in concordance with the “one-hit” model¹⁹. Identification of early disease-associated trends
395 reported herein establishes mitochondria as an integrative node in the cellular response to
396 genetic mutations with a potentially decisive role before the onset of neurodegeneration. We
397 surmise that a mitochondrial link to *rd1* specific PDE6 β mutation, prior to the physiological
398 regulation of cGMP channels, likely results from altered energy homeostasis and abnormal
399 metabolic and calcium signaling. Our findings provide a plausible framework for the etiology of
400 retinal degeneration by incorporating unique photoreceptor ‘omics’ and physiology in concert
401 with our observations from the *rd1* mutant retina. In addition, our studies are consistent with the
402 mechanistic underpinning of neurodegenerative diseases^{62,63} and should have broad
403 implications for deciphering molecular and cellular drivers of disease pathology. Discovery of
404 metabolic and signaling pathways that are altered in anticipation of disease sets the foundation
405 for drug discovery and interventions at an early stage, thereby improving outcomes in clinical
406 management.

407

408

409 **METHODS**

410 **Animal models**

411 Mice were housed in 12-hour light-dark housing conditions and were cared for following
412 recommendations of the Guide for the Care and Use of Laboratory Animals, Institute of
413 Laboratory Animal Resources, the Public Health Service Policy on Humane Care and Use of
414 Laboratory Animals. All mouse protocols have been approved by the Animal Care and Use
415 Committee of the National Eye Institute (ASP#650). The *Pde6b^{rd1/rd1}*; *TgNrlp-EGFP* mice
416 (referred to as *rd1*) were generated by crossing *Pde6b^{rd1/rd1}* mice to *TgNrlp-EGFP* mice until
417 homozygous and maintained as sibling crosses. *TgNrlp-EGFP* mice served as wild type (*WT*)
418 control and were maintained on C57BL/6J backgrounds with >10 backcrosses. Both male and
419 female mice were used in this study.

420 **Retinal histology**

421 After enucleation, eyes were fixed with 4% glutaraldehyde for 30 min at room temperature and
422 then with 4% paraformaldehyde overnight at 4°C. Eyes were then embedded in methacrylate
423 and sectioned at 1-micron thickness. Representative sections from the superior central retina
424 were stained with standard hematoxylin and eosin (H&E) staining protocol. Pictures of retinal
425 section were taken at 40X.

426 **Transcriptomic profiling**

427 ***Flow sorting of rod photoreceptors***

428 Rod photoreceptors from *Pde6b^{rd1/rd1}*; *TgNrlp-GFP (rd1)* and *TgNrlp-GFP (WT)* mice were
429 isolated as previously described³³. In brief, dissected retinas were treated with papain
430 (Worthington Biochemical, NJ, USA) and dissociated single cells were collected by
431 centrifugation at 800 x g for 5 min at 4°C. Cell pellets were resuspended in ice cold PBS. GFP-
432 positive photoreceptor cells were isolated using FACS Aria II (Becton Dickinson, CA, USA) with
433 a stringent precision setting which maximized the purity of sorted cells.

434 **RNA sequencing**

435 Rod photoreceptor cells were lysed with TRIzol LS (Invitrogen), and the RNA was isolated
436 following the manufacturer's instructions. RNAseq data were generated using TruSeq Stranded
437 mRNA Sample Prep Kit (Illumina), as previously described⁶⁴, and 125 base pair-end reads
438 were generated on HiSeq 2500 platform (Illumina).

439 ***Differential RNA expression and downstream analysis***

440 Unprocessed fastq files from the sequencer were quality checked, trimmed and aligned to the
441 *Mus musculus* Ensembl annotation (v98) using a robust pipeline as described before⁶⁴. Briefly,
442 the count matrix was normalized, and batch corrected to generate abundance summary in
443 counts per million using the Bioconductor packages *edgeR* and *limma*. Additionally, to remove
444 artefacts we set an expression filter that required genes to have greater than 5 CPM in minimum
445 two replicates of any sample before qualifying for differential expression analysis. Statistical
446 tests for differential expression between age-matched samples of *rd1* and *WT* were performed
447 with *voom* transformed counts fit to a linear model using functions in *limma*. Finally, a cutoff of
448 10% FDR and 1.5-fold change difference was decided to group genes as differentially
449 expressed genes (DEG). Clusters of DEG were determined from a k-means algorithm after
450 setting a value of k equals 10. Functional enrichment analysis of DEG groups was performed
451 with *gProfileR* and custom scripts where KEGG pathways were ordered by pathway impact, as
452 defined by the ratio between overlap and pathway size. Gene sets for volcano plots were
453 obtained from gProfileR (Reactome), Mouse Genomics Institute (Gene Ontology) and Mitocarta.

454 **Proteomic profiling**

455 ***Retinal tissue lysate processing***

456 Retinal tissues from *WT* and *rd1* mice at P6 and P10 were subject for whole proteomic analysis,
457 performed by core facility at National Heart Lung and Blood Institute. Retinas from 9 non-
458 littermate mice of each sample group were frozen and thawed after dissection, divided in
459 replicates of 6 retinas for each strain and age (n=3 for each group, 12 samples total), and
460 resuspended in 100 μ l of lysis buffer containing 6 M urea, 2 M thiourea and 4% CHAPS

461 (Thermo Fisher Scientific). Each combined replicate of samples was loaded onto a QIAshredder
462 spin column (QIAGEN) placed in a 2 ml collection tube and spun for 2 minutes at maximum
463 speed in a microcentrifuge to aid in tissue disruption. The flow-through for each sample was
464 collected and protein was quantified using the Pierce detergent compatible Bradford assay kit
465 (Thermo Fisher Scientific).

466 A volume corresponding to 100 µg of protein from each replicate, as well as two
467 normalization loading controls generated by pooling 5.55 µg of each replicate were taken to 100
468 µl by adding the necessary volume of lysis buffer. Each resulting sample was reduced by mixing
469 with 5 µl of the 200 mM DTT and incubating at room temperature for 1 hour, and then alkylated
470 by adding 5 µl of 375 mM iodoacetamide and incubating for 30 minutes protected from light at
471 room temperature. Protein in each sample was precipitated by adding 600 µl of pre-chilled
472 acetone and storing overnight at -20°C. Samples were then centrifuged at 8000 × g for 10 min
473 at 4°C, and acetone was carefully decanted without disturbing the white pellet, which was
474 allowed to dry for 2-3 minutes. Each protein pellet was resuspended in 100 µl of a buffer
475 containing 100 mM triethylammonium bicarbonate (TEAB) and 0.1% of Progenta anionic acid-
476 labile surfactant I (AALSI, Protea Biosciences). Each sample was proteolyzed by adding 10 µl of
477 1.25 µg/µl sequencing grade modified trypsin (Promega) dissolved in 100 mM TEAB and
478 incubated overnight at 37°C. Each sample was labeled with a different TMT label reagent
479 (Thermo Fisher Scientific) by adding the contents of each label tube after dissolving with 41 µl of
480 acetonitrile. The reaction was allowed to proceed for 1 hour at room temperature and was
481 quenched by adding 8 µl of 5% hydroxylamine to each sample and incubating for 15 minutes.

482 All seven samples from each strain (6 replicates plus a normalization loading control)
483 were combined in a new microcentrifuge tube, which was dried under vacuum until all
484 acetonitrile was removed. Contaminating CHAPS was removed using 2 ml Pierce detergent
485 removal columns (thermo Fisher Scientific) and residual AALSI was cleaved by adding 30 µl of
486 10% trifluoroacetic acid (TFA). The combined samples were desalted using an Oasis HLB

487 column (Waters) and dried under vacuum.

488 ***Offline HPLC peptide fractionation***

489 High pH reversed-phase liquid chromatography was performed on an offline Agilent 1200 series
490 HPLC. Approximately 1 mg of desalted peptides were resuspended in 0.1 ml of 10 mM triethyl
491 ammonium bicarbonate with 2% (v/v) acetonitrile. Peptides were loaded onto an Xbridge C₁₈
492 HPLC column (Waters; 2.1 mm inner diameter x 100 mm, 5 µm particle size), and profiled with a
493 linear gradient of 5–35 % buffer B (90% acetonitrile, 10 mM triethyl ammonium bicarbonate)
494 over 60 minutes, at a flowrate of 0.25 ml/min. The chromatographic performance was monitored
495 by sampling the eluate with a diode array detector (1200 series HPLC, Agilent) scanning
496 between wavelengths of 200 and 400 nm. Fractions were collected at 1 minute intervals
497 followed by fraction concatenation⁶⁵. Fifteen concatenated fractions were dried and
498 resuspended in 0.01% formic acid, 2% acetonitrile. Approximately 500 ng of peptide mixture
499 was loaded per liquid chromatography-mass spectrometry run.

500 ***Mass Spectrometry (MS)***

501 All fractions were analyzed on an Ultimate 3000-nLC coupled to an Orbitrap Fusion Lumos
502 Tribrid instrument (Thermo Fisher Scientific) equipped with a nanoelectrospray source. Peptides
503 were separated on an EASY-Spray C₁₈ column (75 µm x 50 cm inner diameter, 2 µm particle
504 size and 100 Å pore size, Thermo Fisher Scientific). Peptide fractions were placed in an
505 autosampler and separation was achieved by 90 minutes gradient from 4-35% buffer B (100%
506 ACN and 0.1% formic acid) at a flow rate of 300 nL/min. An electrospray voltage of 1.9 kV was
507 applied to the eluent via the EASY-Spray column electrode. The Lumos was operated in
508 positive ion data-dependent mode, using Synchronous Precursor Selection (SPS-MS3)⁶⁶.

509 Full scan MS1 was performed in the Orbitrap with a precursor selection range of 375 to
510 1,275 m/z at 1.2 x 10⁵ normal resolution. The AGC target and maximum accumulation time
511 settings were set to 4 x 10⁵ and 50 ms, respectively. MS2 was triggered by selecting the
512 most intense precursor ions above an intensity threshold of 5 x 10³ for collision induced

513 dissociation (CID)-MS² fragmentation with an AGC target and maximum accumulation time
514 settings of 1×10^4 and 60 ms, respectively. Mass filtering was performed by the quadrupole
515 with 0.7 m/z transmission window, followed by CID fragmentation in the linear ion trap with 35%
516 normalized collision energy in turbo scan mode and parallelizable time option was selected.
517 SPS was applied to co-select 10 fragment ions for HCD-MS³ analysis. SPS ions were all
518 selected within the 400–1,200 m/z range and were set to preclude selection of the precursor ion
519 and TMTc ion series. The AGC target and maximum accumulation time were set to 1×10^5
520 and 125 ms (respectively) and parallelizable time option was selected. Co-selected precursors
521 for SPS-MS³ underwent HCD fragmentation with 65% normalized collision energy and were
522 analyzed in the Orbitrap with nominal resolution of 5×10^4 . The number of SPS- MS³ spectra
523 acquired between full scans was restricted to a duty cycle of 3 s.

524 ***Mass spectrometry data processing***

525 Raw data files were processed using Proteome Discoverer (v2.4, Thermo Fisher Scientific),
526 using both Mascot (v2.6.2, Matrix Science) and Sequest HT (Thermo Fisher Scientific) search
527 algorithms. All the peak lists were searched against the UniProtKB/Swiss-Prot protein database
528 released 2020_02 with *Mus musculus* taxonomy (17,010 sequences) and concatenated with
529 reversed copies of all sequences. The following search parameters were set as static
530 modifications; carbamidomethylation of cysteine, TMT 10-plex modification of lysine and peptide
531 N-terminus. The variable modifications were set as; oxidation of methionine, deamidation of
532 asparagine and glutamine. For SPS-MS³ the precursor and fragment ion tolerances of 12
533 ppm and 0.5 Da were applied, respectively. Up to two-missed tryptic cleavages were permitted.
534 Percolator (v3.02.1, University of Washington) algorithm was used to calculate the false
535 discovery rate (FDR) of peptide spectrum matches, set to q-value 0.05^{67,68}. TMT 10-plex
536 quantification was also performed by Proteome Discoverer v.2.4 by calculating the sum of
537 centroided ions within 20 ppm window around the expected m/z for each of the 10 TMT reporter
538 ions. Spectra with at least 50% of SPS masses matching to the identified peptide are

539 considered as quantifiable PSMs. Quantification was performed at the MS³ level where the
540 median of all quantifiable PSMs for each protein group was used for protein ratios.

541 ***Differential expression analysis of the proteome***

542 Proteins identified from the MS experiment were filtered to retain only those with at least one
543 unique peptide and that have minimum two peptide spectral matches from either of the two
544 algorithms, MASCOT or Sequest. Further, to classify proteins as differentially expressed, a
545 threshold of 1.2-fold change in both directions of over- and under- expression was decided for
546 age-matched comparisons between *rd1* and *WT*.

547 ***Pathway enrichment analysis of the proteome***

548 GSEA for the proteomic dataset was performed using *fgsea* with ranked fold change values and
549 Reactome and Gene Ontology annotations downloaded from the gProfileR webserver. *Fgsea*
550 significant pathways ($p < 0.05$) were further collapsed to address redundancy. Ridge plots were
551 generated using custom scripts and functions in the *tidyverse* and *ggridges* packages.
552 Additionally, a list of OXPHOS proteins and electron transport chain complexes were curated
553 from literature for use in various analyses.

554 **Metabolomic profiling**

555 ***Retinal metabolome profiling***

556 Targeted quantitative analysis was performed on retinal samples from *WT* and *rd1* mice of P6
557 and P10 to detect cationic and anionic metabolites, using capillary electrophoresis mass
558 spectrometry (CE-TOFMS and CE-QqQMS) in cation and anion analysis modes, respectively,
559 with internal standard (Human Metabolome Technologies). Retinal tissue samples (30-45 mg)
560 were mixed with 50% (v/v) acetonitrile and homogenized and the supernatant obtained after
561 brief centrifugation was filtrated through 5 kDa cut off filter to remove macromolecules. Filtrate
562 was centrifugally concentrated and resuspended in water for mass spectrometry measurement.
563 Metabolite concentrations were calculated by normalizing to internal standard and quantity of

564 sample used. Primary analysis of metabolite detection and abundance estimates were
565 performed by Human Metabolome Technologies, Boston MA.

566 ***Retinal metabolome analysis***

567 For analysis, metabolites were linked to their corresponding KEGG pathways and visualized in a
568 network diagram created with *igraph* (R package) and Cytoscape. To classify differential
569 abundance of metabolites we used two sets of thresholds: a) significance differential abundance
570 with $p < 0.05$ from pairwise tests of age-matched samples at P6 and P10; and b) metabolites with
571 fold change of minimum 1.2 times in either over or under abundance in *rd1* versus *WT*
572 comparisons.

573 **In vitro and ex vivo analysis of mitochondrial activity**

574 ***Complex I activity assay***

575 The protocol for complex I activity assay was adopted from previous publications⁶⁹. In brief,
576 dissected retinas were homogenized in SETH buffer containing 0.25 M sucrose, 2 mM EDTA
577 and 10 mM Tris pH7.4. The lysate was first spun at 600 x g for 10 min at 4°C followed by a
578 second spin of supernatant at 14000 x g for 10 min at 4°C. Mitochondria pellet was
579 resuspended in 10 mM Tris pH7.4. Complex I oxidizes NADH and produces an electron. The
580 produced electron is then used to reduce an artificial substrate decylubiquinone, which
581 subsequently passes the electron to the terminal electron receptor DCIP that is blue in color.
582 Reduction of DCIP concentration can be followed spectrophotometrically at 600nm. Rotenone is
583 added to terminate the reaction and reveal any residue non-complex I related reduction of
584 DCIP.

585 ***Mitochondrial respiration and oxygen consumption***

586 OCR of retinal punches were measured using Seahorse XF24 Bioanalyzer with XF24 Islet
587 Fluxpaks (Agilent) following our published protocol⁹. In brief, eyes were enucleated and placed
588 in ice-cold PBS for dissection. Cornea and lens were removed, and the retinal cup was gently
589 separated away from the scleral layer. Three to four of 1 mm diameter punches equidistant from

590 the optic nerve head were taken from each retina for the measurement. Ames' buffer (Sigma)
591 containing 120 mM NaCl, 10 mM HEPES, pH 7.4 was used in the assay. After steady basal
592 OCR was established, mitochondrial uncoupler (2-fluorophenyl)(6-[(2-fluorophenyl)amino](1,2,5-
593 oxadiazolo[3,4-e]pyrazin-5-yl))amine (BAM15; Timtec, Newark, DE, USA) was added at a final
594 concentration of 5 μ M to uncouple the electrochemical gradient of protons, thereby uncoupling
595 ATP production from oxygen consumption and causing mitochondrial OXPHOS to run at full
596 capacity. The complex I inhibitor rotenone was used at a final concentration of 1 μ M to inhibit
597 the entire electron transport chain and thereby revealing the residual non-mitochondrial oxygen
598 consumption.

599 Raw OCR values were computed by the Seahorse KSV algorithm, per manufacturer's
600 recommendations, and non-mitochondrial oxygen consumption, the residual readings obtained
601 after addition of rotenone, was subtracted from all points. Basal mitochondrial OCR (OCR_{basal})
602 was taken at 36 min, the last measuring point before BAM15 addition, while the highest value
603 from uncoupled points was used for maximal OCR (OCR_{max}). Mitochondrial reserve respiratory
604 capacity (MRC) was calculated as the percentage difference between maximal uncontrolled
605 oxygen consumption rate OCR_{max} and the initial OCR_{basal} : $MRC = \frac{OCR_{\text{max}} - OCR_{\text{basal}}}{OCR_{\text{max}}} \times 100\%$. A
606 range of 4 to 8 non-littermate animals were included in each age group of *WT* and *rd1* mice, and
607 data from 12~29 retinal punches were included for analysis in each age/genotype group. Group
608 means \pm SEMs are plotted for each age group and strain.

609 **Transmission Electron Microscopy**

610 The mitochondrial ultrastructure was evaluated by transmission electron microscopy (TEM)
611 following standard preparation procedures⁷⁰. Eyes were enucleated and immersion fixed in 1%
612 paraformaldehyde, 2.5% glutaraldehyde in PBS (pH 7.4), followed by treatment with 1%
613 osmium tetroxide. Fixed samples were dehydrated through a series of ethanol gradient and in
614 propylene oxide, and then embedded in epoxy resin. The retina samples were sectioned at 80-

615 90 nm, mounted on copper grids, and doubly stained with uranyl acetate and lead citrate.

616 Sections were imaged at the NEI Histology Core with JEOL JEM-1010 TEM. Photographs were
617 taken for the inner segment region of the photoreceptors at 10,000x and 30,000x
618 magnifications.

619 **qPCR and Mit/Nu DNA ratio**

620 The Mit/Nu DNA ratio were determined on P2 to P10 retinal samples from *WT* and *rd1* mice
621 using a published protocol³⁷. Whole genomic DNA was isolated from retinal tissues and
622 quantitative PCR on the genomic DNA abundance of mitochondria-encoded *Nd1* and nucleus-
623 encoded *Hk2* was performed to evaluate copy number of mitochondrial and nuclear genome
624 respectively. The mtDNA to nuDNA ratio was calculated by a $\Delta\Delta\text{Ct}$ method.

625 **Quantification and statistical analysis**

626 Unless specified otherwise, all statistical analyses and data visualizations were done using the
627 R statistical platform. Differences from *WT* were regarded as significant if $p < 0.05$.

628

629

630

631 **ACKNOWLEDGMENTS**

632 We are grateful to Yide Mi, Ashley Yedlicka and Megan Kopera for mouse colony management;
633 Julie Laux, Jessica Albrecht and Rafael Villasmil of the NEI flow cytometry core for their
634 assistance; and Thad Whitaker, Maria Campos, Mones Abu-Asab and the NEI histology core for
635 histology and TEM. This research was supported by Intramural Research Program of the NEI
636 (ZIAEY000450 and ZIAEY000546) and utilized the high-performance computational capabilities
637 of the Biowulf Linux cluster at NIH (<http://biowulf.nih.gov>).

638

639 **Author Contributions**

640 Overall Conceptualization, K.J., J.W.K., A.K.M., R.C. and A.S.; Methodology and Investigation,
641 K.J., Y.A., J.G., J.W.K., A.B., J.N.; Omics Data Generation and Analysis, A.K.M., A.A., L.G.,
642 M.J.B., R.C.; Data Curation, A.K.M.; Resources, K.J., D.A.F., R.B., R.C., Writing – Original Draft,
643 K.J., A.K.M., A.S.; Writing – Review & Editing, all authors; Supervision, R.C., A.S.; Funding
644 Acquisition and Project Administration, A.S.

645

646 **Competing Interests**

647 The authors declare no competing interests.

648

649 **Materials and Correspondence**

650 Correspondence and material requests should be addressed to Anand Swaroop, Ph.D.,
651 Neurobiology-Neurodegeneration & Repair Laboratory, National Eye Institute, National Institutes
652 of Health, MSC0610, 6 Center Drive, Bethesda, MD, USA. Phone: 301.435.5754; Fax:
653 301.480.9917; E-mail: swaroopa@nei.nih.gov

654

655

656

657 REFERENCES

- 658 1 Parikshak, N. N., Gandal, M. J. & Geschwind, D. H. Systems biology and gene networks
659 in neurodevelopmental and neurodegenerative disorders. *Nat Rev Genet* **16**, 441-458,
660 doi:10.1038/nrg3934 (2015).
- 661 2 Gan, L., Cookson, M. R., Petrucelli, L. & La Spada, A. R. Converging pathways in
662 neurodegeneration, from genetics to mechanisms. *Nature neuroscience* **21**, 1300-1309,
663 doi:10.1038/s41593-018-0237-7 (2018).
- 664 3 Menzies, F. M., Fleming, A. & Rubinsztein, D. C. Compromised autophagy and
665 neurodegenerative diseases. *Nature reviews. Neuroscience* **16**, 345-357,
666 doi:10.1038/nrn3961 (2015).
- 667 4 Verdin, E. NAD(+) in aging, metabolism, and neurodegeneration. *Science (New York,*
668 *N.Y.)* **350**, 1208-1213, doi:10.1126/science.aac4854 (2015).
- 669 5 Wolozin, B. & Ivanov, P. Stress granules and neurodegeneration. *Nature reviews.*
670 *Neuroscience* **20**, 649-666, doi:10.1038/s41583-019-0222-5 (2019).
- 671 6 Wright, A. F. *et al.* Lifespan and mitochondrial control of neurodegeneration. *Nature*
672 *genetics* **36**, 1153-1158, doi:10.1038/ng1448 (2004).
- 673 7 Lin, M. T. & Beal, M. F. Mitochondrial dysfunction and oxidative stress in
674 neurodegenerative diseases. *Nature* **443**, 787-795, doi:10.1038/nature05292 (2006).
- 675 8 Hasson, S. A. *et al.* High-content genome-wide RNAi screens identify regulators of
676 parkin upstream of mitophagy. *Nature* **504**, 291-295, doi:10.1038/nature12748 (2013).
- 677 9 Kooragayala, K. *et al.* Quantification of Oxygen Consumption in Retina Ex Vivo
678 Demonstrates Limited Reserve Capacity of Photoreceptor Mitochondria. *Investigative*
679 *ophthalmology & visual science* **56**, 8428-8436, doi:10.1167/iovs.15-17901 (2015).
- 680 10 Ducker, G. S. & Rabinowitz, J. D. One-Carbon Metabolism in Health and Disease. *Cell*
681 *Metab* **25**, 27-42, doi:10.1016/j.cmet.2016.08.009 (2017).
- 682 11 Yang, L. *et al.* Serine Catabolism Feeds NADH when Respiration Is Impaired. *Cell*
683 *Metab* **31**, 809-821 e806, doi:10.1016/j.cmet.2020.02.017 (2020).
- 684 12 Hanany, M., Rivolta, C. & Sharon, D. Worldwide carrier frequency and genetic
685 prevalence of autosomal recessive inherited retinal diseases. *Proceedings of the*
686 *National Academy of Sciences of the United States of America* **117**, 2710-2716,
687 doi:10.1073/pnas.1913179117 (2020).
- 688 13 Perea-Romero, I. *et al.* Genetic landscape of 6089 inherited retinal dystrophies affected
689 cases in Spain and their therapeutic and extended epidemiological implications. *Sci Rep*
690 **11**, 1526, doi:10.1038/s41598-021-81093-y (2021).
- 691 14 Roska, B. & Sahel, J. A. Restoring vision. *Nature* **557**, 359-367, doi:10.1038/s41586-
692 018-0076-4 (2018).
- 693 15 Garafalo, A. V. *et al.* Progress in treating inherited retinal diseases: Early subretinal gene
694 therapy clinical trials and candidates for future initiatives. *Prog Retin Eye Res* **77**,
695 100827, doi:10.1016/j.preteyeres.2019.100827 (2020).
- 696 16 Travis, G. H. Mechanisms of cell death in the inherited retinal degenerations. *Am J Hum*
697 *Genet* **62**, 503-508, doi:10.1086/301772 (1998).
- 698 17 Power, M. *et al.* Cellular mechanisms of hereditary photoreceptor degeneration - Focus
699 on cGMP. *Prog Retin Eye Res* **74**, 100772, doi:10.1016/j.preteyeres.2019.07.005
700 (2020).
- 701 18 Sanges, D., Comitato, A., Tammara, R. & Marigo, V. Apoptosis in retinal degeneration
702 involves cross-talk between apoptosis-inducing factor (AIF) and caspase-12 and is
703 blocked by calpain inhibitors. *Proceedings of the National Academy of Sciences of the*
704 *United States of America* **103**, 17366-17371, doi:10.1073/pnas.0606276103 (2006).
- 705 19 Clarke, G. *et al.* A one-hit model of cell death in inherited neuronal degenerations.
706 *Nature* **406**, 195-199, doi:10.1038/35018098 (2000).

- 707 20 Swaroop, A., Kim, D. & Forrest, D. Transcriptional regulation of photoreceptor
708 development and homeostasis in the mammalian retina. *Nature reviews. Neuroscience*
709 **11**, 563-576, doi:10.1038/nrn2880 (2010).
- 710 21 Wright, A. F., Chakarova, C. F., Abd El-Aziz, M. M. & Bhattacharya, S. S. Photoreceptor
711 degeneration: genetic and mechanistic dissection of a complex trait. *Nat Rev Genet* **11**,
712 273-284, doi:10.1038/nrg2717 (2010).
- 713 22 Veleri, S. *et al.* Biology and therapy of inherited retinal degenerative disease: insights
714 from mouse models. *Dis Model Mech* **8**, 109-129, doi:10.1242/dmm.017913 (2015).
- 715 23 Collin, G. B. *et al.* Mouse Models of Inherited Retinal Degeneration with Photoreceptor
716 Cell Loss. *Cells* **9**, doi:10.3390/cells9040931 (2020).
- 717 24 Bowes, C. *et al.* Retinal degeneration in the rd mouse is caused by a defect in the beta
718 subunit of rod cGMP-phosphodiesterase. *Nature* **347**, 677-680, doi:10.1038/347677a0
719 (1990).
- 720 25 Pittler, S. J. & Baehr, W. Identification of a nonsense mutation in the rod photoreceptor
721 cGMP phosphodiesterase beta-subunit gene of the rd mouse. *Proceedings of the*
722 *National Academy of Sciences of the United States of America* **88**, 8322-8326,
723 doi:10.1073/pnas.88.19.8322 (1991).
- 724 26 Watanabe, S. & Matthews, G. Regional distribution of cGMP-activated ion channels in
725 the plasma membrane of the rod photoreceptor. *J Neurosci* **8**, 2334-2337 (1988).
- 726 27 Palczewski, K. Chemistry and biology of the initial steps in vision: the Friedenwald
727 lecture. *Investigative ophthalmology & visual science* **55**, 6651-6672,
728 doi:10.1167/iovs.14-15502 (2014).
- 729 28 McLaughlin, M. E., Sandberg, M. A., Berson, E. L. & Dryja, T. P. Recessive mutations in
730 the gene encoding the beta-subunit of rod phosphodiesterase in patients with retinitis
731 pigmentosa. *Nature genetics* **4**, 130-134, doi:10.1038/ng0693-130 (1993).
- 732 29 Punzo, C., Xiong, W. & Cepko, C. L. Loss of daylight vision in retinal degeneration: are
733 oxidative stress and metabolic dysregulation to blame? *J Biol Chem* **287**, 1642-1648,
734 doi:10.1074/jbc.R111.304428 (2012).
- 735 30 Kanow, M. A. *et al.* Biochemical adaptations of the retina and retinal pigment epithelium
736 support a metabolic ecosystem in the vertebrate eye. *eLife* **6**, doi:10.7554/eLife.28899
737 (2017).
- 738 31 Park, K. S., Xu, C. L., Cui, X. & Tsang, S. H. Reprogramming the metabolome rescues
739 retinal degeneration. *Cell Mol Life Sci* **75**, 1559-1566, doi:10.1007/s00018-018-2744-9
740 (2018).
- 741 32 Akimoto, M. *et al.* Targeting of GFP to newborn rods by Nrl promoter and temporal
742 expression profiling of flow-sorted photoreceptors. *Proceedings of the National Academy*
743 *of Sciences of the United States of America* **103**, 3890-3895,
744 doi:10.1073/pnas.0508214103 (2006).
- 745 33 Kim, J. W. *et al.* NRL-Regulated Transcriptome Dynamics of Developing Rod
746 Photoreceptors. *Cell reports* **17**, 2460-2473, doi:10.1016/j.celrep.2016.10.074 (2016).
- 747 34 Borowski, L. S., Szczesny, R. J., Brzezniak, L. K. & Stepien, P. P. RNA turnover in
748 human mitochondria: more questions than answers? *Biochim Biophys Acta* **1797**, 1066-
749 1070, doi:10.1016/j.bbabi.2010.01.028 (2010).
- 750 35 Kohn, L. *et al.* Mutation in the PYK2-binding domain of PIP3 causes autosomal
751 dominant cone dystrophy (CORD5) in two Swedish families. *European journal of human*
752 *genetics : EJHG* **15**, 664-671, doi:10.1038/sj.ejhg.5201817 (2007).
- 753 36 Boldyrev, A. A., Aldini, G. & Derave, W. Physiology and pathophysiology of carnosine.
754 *Physiol Rev* **93**, 1803-1845, doi:10.1152/physrev.00039.2012 (2013).
- 755 37 Quiros, P. M., Goyal, A., Jha, P. & Auwerx, J. Analysis of mtDNA/nDNA Ratio in Mice.
756 *Curr Protoc Mouse Biol* **7**, 47-54, doi:10.1002/cpmo.21 (2017).

- 757 38 Jackson, G. R., Owsley, C. & Curcio, C. A. Photoreceptor degeneration and dysfunction
758 in aging and age-related maculopathy. *Ageing Res Rev* **1**, 381-396 (2002).
- 759 39 Ait-Ali, N. *et al.* Rod-derived cone viability factor promotes cone survival by stimulating
760 aerobic glycolysis. *Cell* **161**, 817-832, doi:10.1016/j.cell.2015.03.023 (2015).
- 761 40 Xu, J. *et al.* cGMP accumulation causes photoreceptor degeneration in CNG channel
762 deficiency: evidence of cGMP cytotoxicity independently of enhanced CNG channel
763 function. *J Neurosci* **33**, 14939-14948, doi:10.1523/JNEUROSCI.0909-13.2013 (2013).
- 764 41 Wang, T., Tsang, S. H. & Chen, J. Two pathways of rod photoreceptor cell death
765 induced by elevated cGMP. *Human molecular genetics* **26**, 2299-2306,
766 doi:10.1093/hmg/ddx121 (2017).
- 767 42 Vinberg, F., Chen, J. & Kefalov, V. J. Regulation of calcium homeostasis in the outer
768 segments of rod and cone photoreceptors. *Prog Retin Eye Res* **67**, 87-101,
769 doi:10.1016/j.preteyeres.2018.06.001 (2018).
- 770 43 Okawa, H., Sampath, A. P., Laughlin, S. B. & Fain, G. L. ATP consumption by
771 mammalian rod photoreceptors in darkness and in light. *Curr Biol* **18**, 1917-1921,
772 doi:10.1016/j.cub.2008.10.029 (2008).
- 773 44 Rueda, E. M. *et al.* The cellular and compartmental profile of mouse retinal glycolysis,
774 tricarboxylic acid cycle, oxidative phosphorylation, and ~P transferring kinases.
775 *Molecular vision* **22**, 847-885 (2016).
- 776 45 Venkatesh, A. *et al.* Activated mTORC1 promotes long-term cone survival in retinitis
777 pigmentosa mice. *J Clin Invest* **125**, 1446-1458, doi:10.1172/JCI79766 (2015).
- 778 46 Zhang, L. *et al.* Reprogramming metabolism by targeting sirtuin 6 attenuates retinal
779 degeneration. *J Clin Invest* **126**, 4659-4673, doi:10.1172/JCI86905 (2016).
- 780 47 Xue, Y. *et al.* AAV-Txnip prolongs cone survival and vision in mouse models of retinitis
781 pigmentosa. *eLife* **10**, doi:10.7554/eLife.66240 (2021).
- 782 48 Perkins, G. A., Ellisman, M. H. & Fox, D. A. Three-dimensional analysis of mouse rod
783 and cone mitochondrial cristae architecture: bioenergetic and functional implications.
784 *Molecular vision* **9**, 60-73 (2003).
- 785 49 Vlachantoni, D. *et al.* Evidence of severe mitochondrial oxidative stress and a protective
786 effect of low oxygen in mouse models of inherited photoreceptor degeneration. *Human*
787 *molecular genetics* **20**, 322-335, doi:10.1093/hmg/ddq467 (2011).
- 788 50 Nicholls, D. G. Mitochondrial ion circuits. *Essays Biochem* **47**, 25-35,
789 doi:10.1042/bse0470025 (2010).
- 790 51 Klaus, S. & Ost, M. Mitochondrial uncoupling and longevity - A role for mitokines? *Exp*
791 *Gerontol* **130**, 110796, doi:10.1016/j.exger.2019.110796 (2020).
- 792 52 Perron, N. R., Beeson, C. & Rohrer, B. Early alterations in mitochondrial reserve
793 capacity; a means to predict subsequent photoreceptor cell death. *J Bioenerg Biomembr*
794 **45**, 101-109, doi:10.1007/s10863-012-9477-5 (2013).
- 795 53 Fox, D. A., Poblenz, A. T. & He, L. Calcium overload triggers rod photoreceptor
796 apoptotic cell death in chemical-induced and inherited retinal degenerations. *Ann N Y*
797 *Acad Sci* **893**, 282-285, doi:10.1111/j.1749-6632.1999.tb07837.x (1999).
- 798 54 Glancy, B. & Balaban, R. S. Role of mitochondrial Ca²⁺ in the regulation of cellular
799 energetics. *Biochemistry* **51**, 2959-2973, doi:10.1021/bi2018909 (2012).
- 800 55 He, L., Poblenz, A. T., Medrano, C. J. & Fox, D. A. Lead and calcium produce rod
801 photoreceptor cell apoptosis by opening the mitochondrial permeability transition pore. *J*
802 *Biol Chem* **275**, 12175-12184, doi:10.1074/jbc.275.16.12175 (2000).
- 803 56 Petit, L. *et al.* Aerobic Glycolysis Is Essential for Normal Rod Function and Controls
804 Secondary Cone Death in Retinitis Pigmentosa. *Cell reports* **23**, 2629-2642,
805 doi:10.1016/j.celrep.2018.04.111 (2018).

- 806 57 Pilkis, S. J., Claus, T. H., Kurland, I. J. & Lange, A. J. 6-Phosphofructo-2-
807 kinase/fructose-2,6-bisphosphatase: a metabolic signaling enzyme. *Annual review of*
808 *biochemistry* **64**, 799-835, doi:10.1146/annurev.bi.64.070195.004055 (1995).
- 809 58 Randle, P. J. Fuel selection in animals. *Biochem Soc Trans* **14**, 799-806,
810 doi:10.1042/bst0140799 (1986).
- 811 59 Rowe, A. A., Patel, P. D., Gordillo, R. & Wert, K. J. Replenishment of TCA cycle
812 intermediates provides photoreceptor resilience against neurodegeneration during
813 progression of retinitis pigmentosa. *JCI Insight*, doi:10.1172/jci.insight.150898 (2021).
- 814 60 Yuan, T., Walsh, M. P., Sutherland, C., Fabian, H. & Vogel, H. J. Calcium-dependent
815 and -independent interactions of the calmodulin-binding domain of cyclic nucleotide
816 phosphodiesterase with calmodulin. *Biochemistry* **38**, 1446-1455,
817 doi:10.1021/bi9816453 (1999).
- 818 61 Hsu, Y. T. & Molday, R. S. Interaction of calmodulin with the cyclic GMP-gated channel
819 of rod photoreceptor cells. Modulation of activity, affinity purification, and localization. *J*
820 *Biol Chem* **269**, 29765-29770 (1994).
- 821 62 Godoy, J. A. *et al.* Mitostasis, Calcium and Free Radicals in Health, Aging and
822 Neurodegeneration. *Biomolecules* **11**, doi:10.3390/biom11071012 (2021).
- 823 63 Area-Gomez, E., Guardia-Laguarta, C., Schon, E. A. & Przedborski, S. Mitochondria,
824 OxPhos, and neurodegeneration: cells are not just running out of gas. *J Clin Invest* **129**,
825 34-45, doi:10.1172/JCI120848 (2019).
- 826 64 Brooks, M. J. *et al.* Improved Retinal Organoid Differentiation by Modulating Signaling
827 Pathways Revealed by Comparative Transcriptome Analyses with Development In Vivo.
828 *Stem Cell Reports* **13**, 891-905, doi:10.1016/j.stemcr.2019.09.009 (2019).
- 829 65 Yang, F., Shen, Y., Camp, D. G., 2nd & Smith, R. D. High-pH reversed-phase
830 chromatography with fraction concatenation for 2D proteomic analysis. *Expert Rev*
831 *Proteomics* **9**, 129-134, doi:10.1586/epr.12.15 (2012).
- 832 66 Ting, L., Rad, R., Gygi, S. P. & Haas, W. MS3 eliminates ratio distortion in isobaric
833 multiplexed quantitative proteomics. *Nat Methods* **8**, 937-940, doi:10.1038/nmeth.1714
834 (2011).
- 835 67 Brosch, M., Yu, L., Hubbard, T. & Choudhary, J. Accurate and sensitive peptide
836 identification with Mascot Percolator. *J Proteome Res* **8**, 3176-3181,
837 doi:10.1021/pr800982s (2009).
- 838 68 Spivak, M., Weston, J., Bottou, L., Kall, L. & Noble, W. S. Improvements to the
839 percolator algorithm for Peptide identification from shotgun proteomics data sets. *J*
840 *Proteome Res* **8**, 3737-3745, doi:10.1021/pr801109k (2009).
- 841 69 Janssen, A. J. *et al.* Spectrophotometric assay for complex I of the respiratory chain in
842 tissue samples and cultured fibroblasts. *Clin Chem* **53**, 729-734,
843 doi:10.1373/clinchem.2006.078873 (2007).
- 844 70 Ogilvy, A. J., Shen, D., Wang, Y., Chan, C.-C. & Abu-Asab, M. S. Implications of DNA
845 leakage in eyes of mutant mice. *Ultrastruct Pathol* **38**, 335-343,
846 doi:10.3109/01913123.2014.927406 (2014).
- 847

849 **FIGURE LEGENDS**

850 **Figure 1. Transcriptome dynamics of rod photoreceptors prior to cell death in the *rd1***
851 **retina.**

- 852 A. Pathology in the *rd1* retina and study design. Representative histology pictures of retinal
853 cross sections from *WT* and *rd1* mice at ages ranging from P8 to P14 (Top panel). A
854 schematic summary of timeline showing development in *WT* retina and onset of
855 degeneration in *rd1* (Middle panel). Experimental plan and ages of sampling for each
856 assay (Bottom panel). Scale bar = 20 μm . OS: outer segment, IS: inner segment, ONL:
857 outer nuclear layer, INL: inner nuclear layer, GC: ganglion cell.
- 858 B. Principal Component Analysis (PCA) plot summarizing the transcriptomic landscape of
859 rod photoreceptors of *WT* and *rd1* retina.
- 860 C. Trend of differential gene expression between *WT* and *rd1* rods. The number atop each
861 bar represents the total number of significantly differentially expressed genes (DEGs) in
862 a pairwise comparison between age-matched *WT* and *rd1* samples.
- 863 D. Heatmap of gene expression of all DEGs that are significant across age-matched
864 comparisons. Log CPM (lcpm) values are row scaled to z-scores for plotting. See also
865 Figure S1D.
- 866 E. Heatmaps of gene expression of significant DEGs that participate in glucose metabolism
867 (glycolysis, oxidative phosphorylation, pentose phosphate) and purine metabolism
868 pathways. Log CPM (lcpm) values are row scaled to z-scores for plotting. Color scale
869 bar is same as in Figure 1D. See also Figure S2.

870

871 **Figure 2. Proteomics identifies dysregulation of Electron Transport Chain complex I in**
872 **the *rd1* retina before degeneration onset.**

- 873 A. Venn diagram comparison of differentially expressed proteins in P6 and P10 *rd1* retina.

- 874 B. Summary of pathway enrichment analysis that identifies differential regulation at early
875 stages (P6) in the *rd1* retina. Ridge-plots show fold change (*rd1* vs *WT*) distribution of
876 leading-edge proteins from significant genesets. The top and bottom panels show over-
877 and under-enriched pathways in red and blue colors respectively. See also Figure S3B
878 for late stage (P10) data.
- 879 C. Proteomic fold change (FC) of mitochondrial electron transport chain complexes. Black
880 dots inside violin plots represent significant differential expression of an individual protein
881 (*rd1* vs *WT*) of a specific complex. Gray dots inside violin plots represent non-significant
882 differential expression.
- 883 D. Dumb bell plot showing change in protein expression from P6 to P10 for leading-edge
884 proteins of oxidative phosphorylation. Dark red and purple dots represent significantly
885 different proteins at P6 and P10, respectively. Grayed dots represent proteins with
886 expression less than statistical significance threshold. See also Figure S3C.

887

888 **Figure 3. *rd1* retinas harbor abnormal abundance of mitochondrial and calcium related**
889 **proteins before degeneration.**

- 890 A. Scatter plot of manually curated mitochondrial proteins show differential regulation of
891 mitochondrial metabolic and signaling proteins at P6 and P10. Proteins with
892 abundances significantly different at P6, P10, and both P6 and P10 are labeled in
893 red, blue, and brown, respectively.
- 894 B. Dumb bell plot showing change in protein expression from P6 to P10 for significantly
895 differential glycolysis, TCA and PPP proteins. Dark red and purple dots denote
896 proteins above significance threshold at P6 and P10, respectively. Gray dots
897 represent proteins with non-significant differential expression.
- 898 C. Phosphopeptides detected in pyruvate dehydrogenase (PDH) E1 alpha subunit.

899 D. Dumb bell plot showing change in protein expression from P6 to P10 for significantly
900 differential calcium related proteins. Plot on the left summarizes proteins over-
901 expressed in the *rd1* retina, whereas plot on the right depicts under-expressed
902 proteins. Color codes are same as in Figure 3B.

903

904 **Figure 4. Global metabolite profiling identifies aberrant central carbon metabolism.**

- 905 A. Relative abundance plot for the metabolome of the *rd1* retina relative to *WT*, at P6,
906 showing the highest and least abundant metabolites. See also Figure S4A for P10 data.
- 907 B. Mapping of identified metabolites to KEGG pathways. Significantly altered metabolites at
908 P6 in *rd1* relative to *WT* retinas are colored in either red or blue corresponding to
909 increased or decreased abundance, respectively, while pathways are shown in grey.
910 The top five pathways with the most significantly different metabolites are labeled and
911 highlighted in yellow. Grey dots are metabolites with differential abundance level less
912 than statistical significance threshold.
- 913 C. Annotated pathway diagram and connections between glycolysis, PPP, and purine
914 metabolism, with differential metabolites at P6 highlighted. Metabolites with significantly
915 different abundance ($p < 0.05$) are highlighted in dark blue, while those showing only
916 differential abundance higher than fold change threshold (> 1.2 fold) are highlighted in
917 light blue. Black colored metabolites are detected but do not show differential
918 abundance, while gray colored metabolites were not detected in the metabolomic
919 analysis. Red and black colors in metabolite abundance plots represent *rd1* and *WT*,
920 respectively. Significantly altered metabolites are marked with an asterisk (see STAR
921 Methods for details).
- 922 D. Abundance levels of adenine and guanine and their corresponding nucleotides at P6.
923 Color and significance features are same as Figure 4C.

924 E. Sum of metabolites involved in glycolysis and PPP in the *rd1* retina at P6. Color and
925 significance features are same as Figure 4C. See also Figure S4B for P10 data.

926

927 **Figure 5. Early functional aberrations in mitochondria before the onset of photoreceptor**
928 **degeneration in *rd1* retina.**

929 A. Traces of mitochondrial OCR in retinal punches isolated from *WT* and *rd1* mice at
930 various ages from P3 to P14 (n=12 to 29 retinal punches, for each group). BAM15 and
931 rotenone were added at indicated time during experiments. Data are represented as
932 mean \pm SEM.

933 B. Basal mitochondrial OCR in *WT* and *rd1* retinal punches at each age tested. Values
934 were taken at 36 min, right before addition of BAM15. Plot of mitochondrial reserve
935 capacity in *WT* and *rd1* retinal punches at each age tested. Data are represented as
936 mean \pm SEM. Student t test, * $p < 0.05$, ** $p < 0.01$, *** $p < 0.001$.

937

938 **Figure 6. Mitochondrial ultrastructural alterations at early stages before photoreceptor**
939 **degeneration in *rd1* retinas.**

940 TEM of photoreceptor inner segment area from P6 to P10 *WT* and *rd1* retina are shown at
941 magnifications of 10,000x and 30,000x (zoomed-in area, indicated by white square box). Red
942 arrowheads indicate abnormal mitochondria with swollen cristae. Scale bar = 2 μ m. See also
943 Figure S6.

944

945 **Figure 7. An integrated mitochondria-centered model of molecular events leading to**
946 **photoreceptor cell death in retinal degeneration.** Altered gene expression starts in newborn
947 *rd1* rod photoreceptors carrying the *Pde6b* mutation. Differentially expressed key enzymes
948 (MTHFR and AHCY) affect the balance of one-carbon metabolism, which in turn influences
949 nucleic acid synthesis and pan-methylation status. Concurrently, reduced calmodulin expression

950 leads to dysregulation of calcium-mediated signaling. Increased intracellular calcium enters
951 mitochondria, activates PDP, which in turn stimulates PDC by enhancing its dephosphorylation.
952 Faster consumption of pyruvate triggers an imbalance of the metabolite pool in glycolysis and
953 pentose pathways. Higher calcium also increases damage to mitochondria, which are replaced
954 more rapidly by accelerated degradation and biogenesis (turnover). Enhanced biosynthesis of
955 mitochondrial membrane phospholipids would further deplete glycolytic intermediates. Lower
956 complex I activity is compensated by increased electron transfer from fatty acid, aspartate and
957 leucine metabolism into the UQ pool. These changes lead to enhanced OCR, reduction in MRC,
958 and increase in cytosolic ATP. With progressive imbalance in metabolism and augmented
959 stress, mitochondria and their cristae swell and rupture, eventually committing the cell to a
960 death fate. UQ: ubiquinone, Dho DH: dihydroorotate dehydrogenase, Iv DH: isovaleryl-CoA
961 dehydrogenase, PDC: pyruvate dehydrogenase complex, PDP: pyruvate dehydrogenase
962 phosphatase, PDK: pyruvate dehydrogenase kinase.
963
964

Figure 1

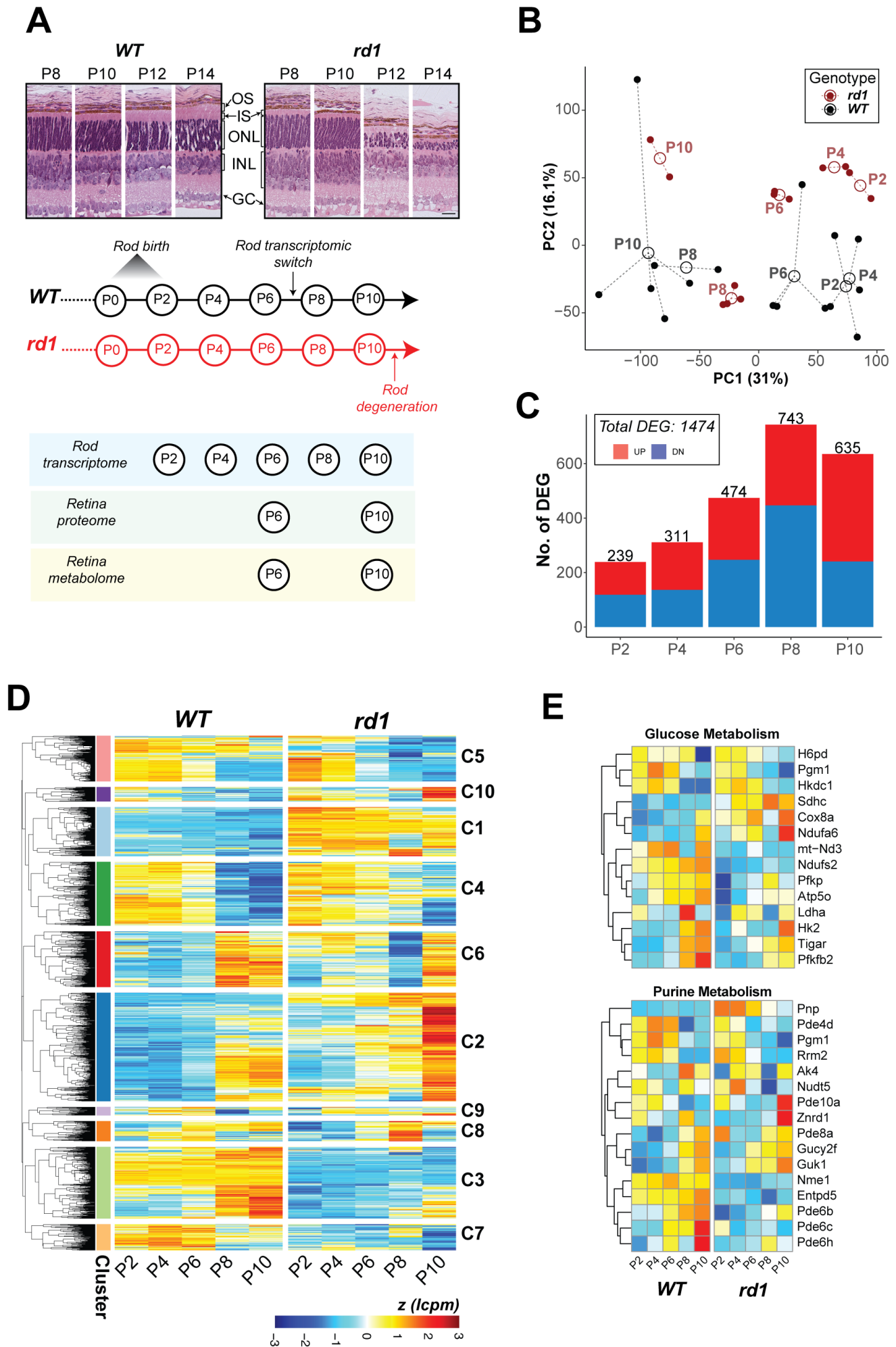
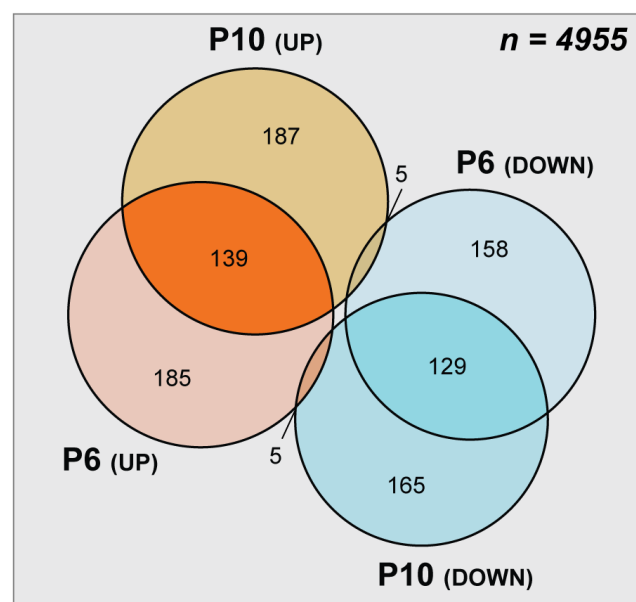
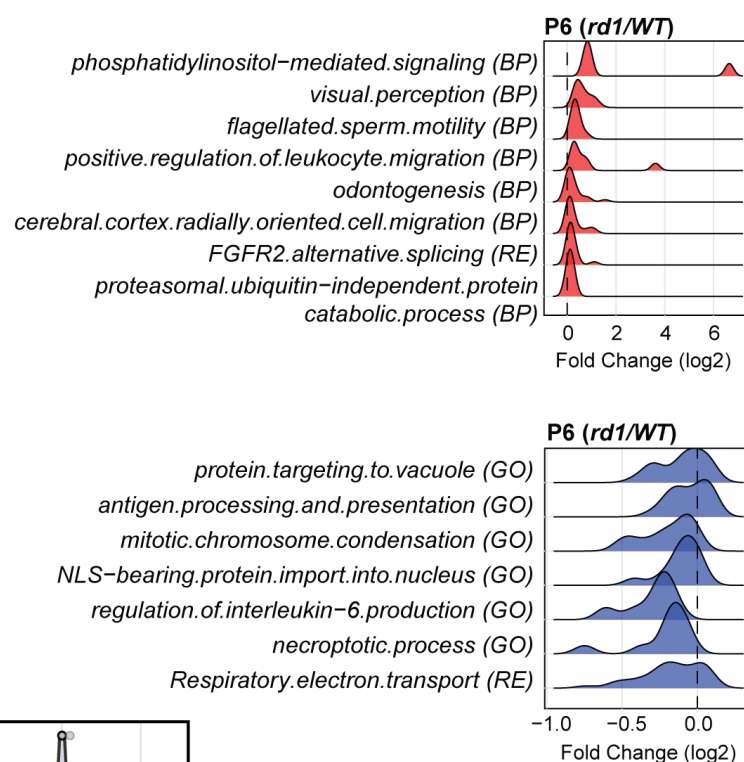


Figure 2

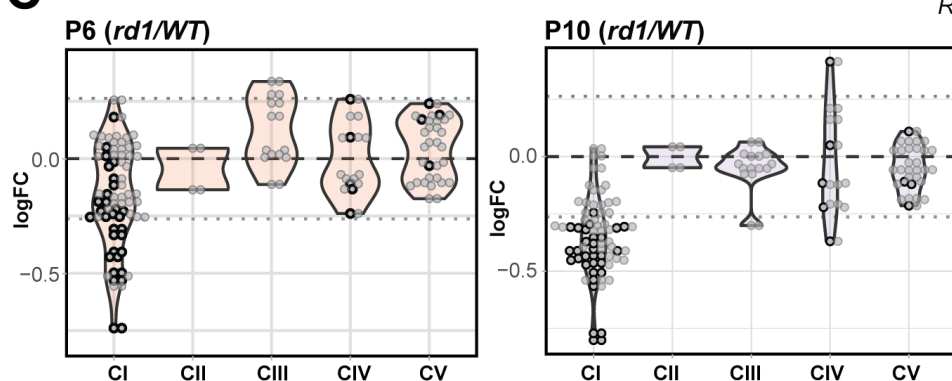
A



B

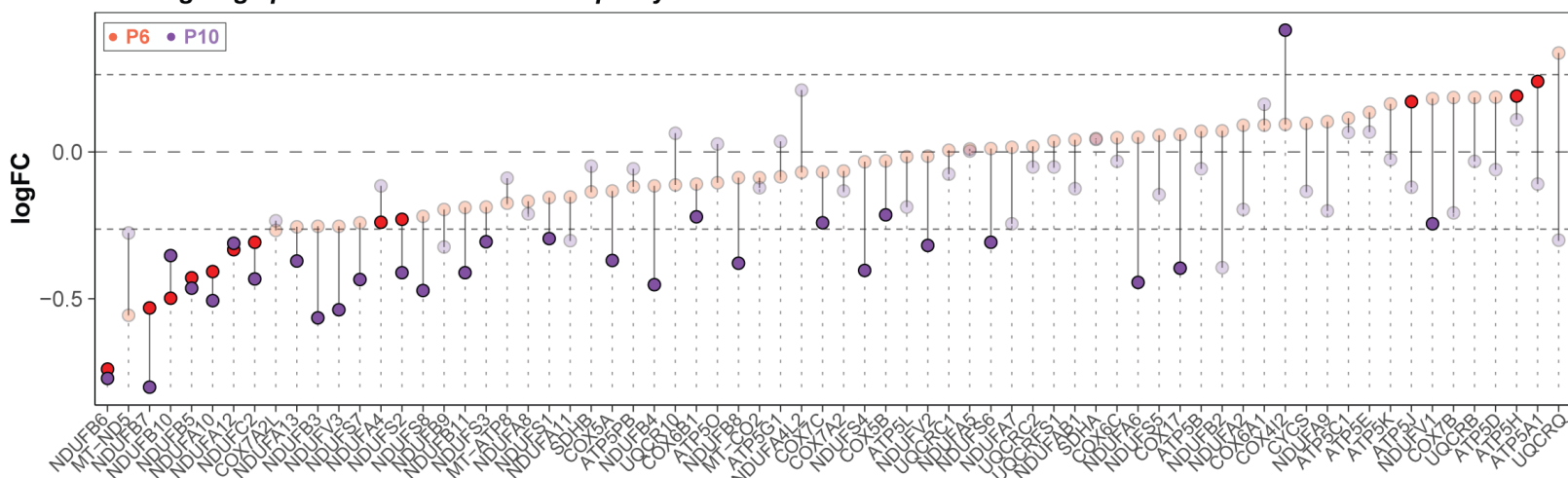


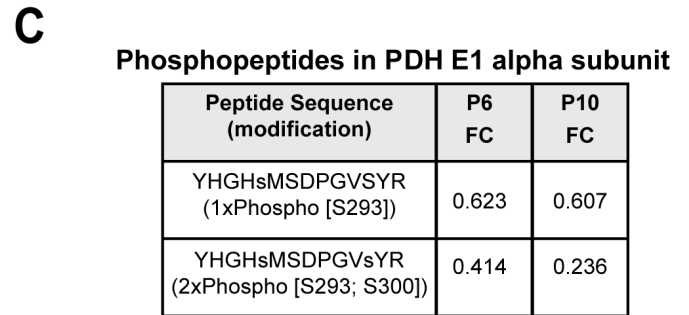
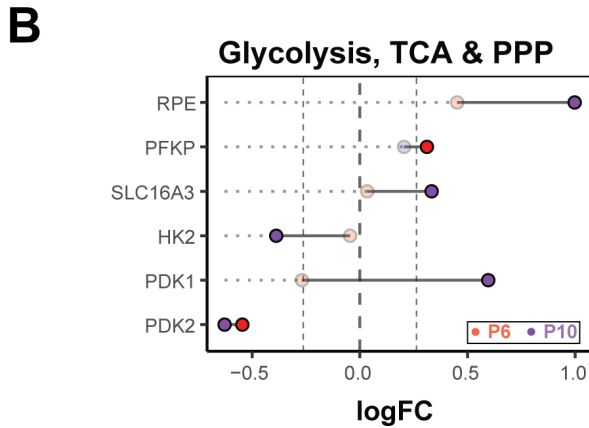
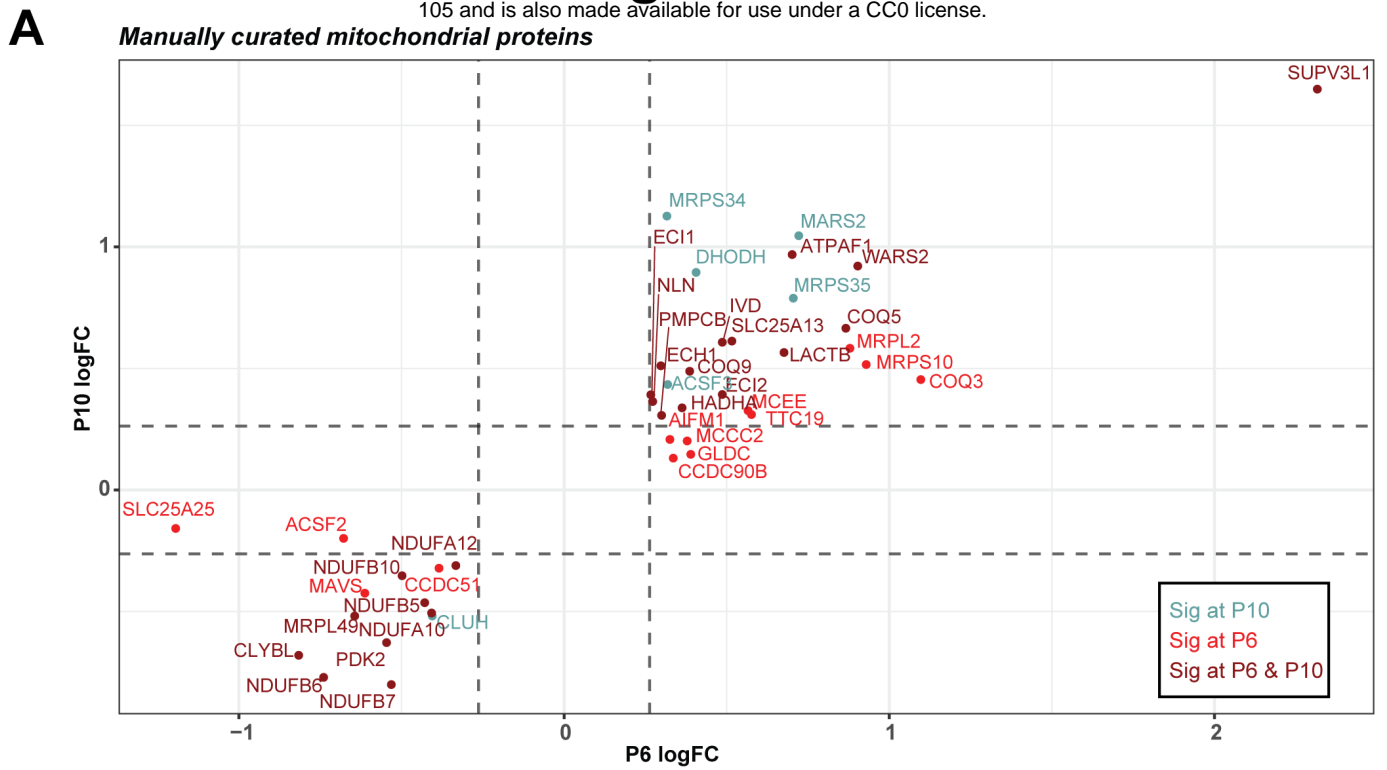
C



D

Leading Edge proteins of Oxidative Phosphorylation





D **Calcium related proteins**

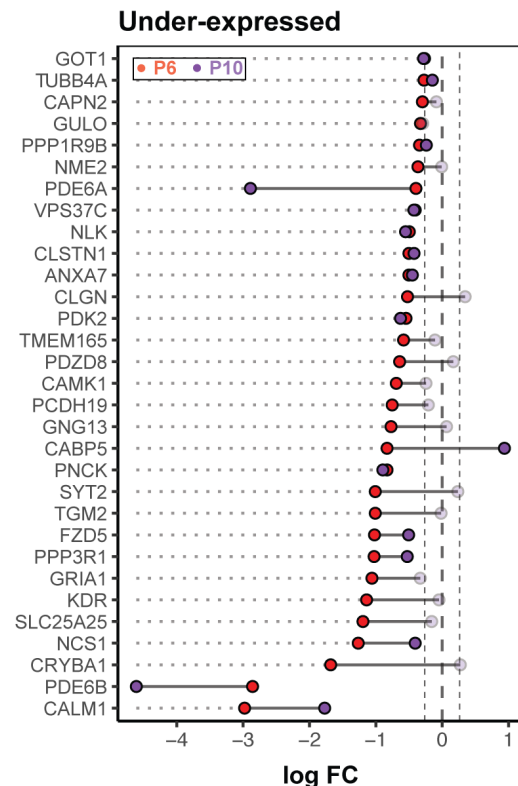
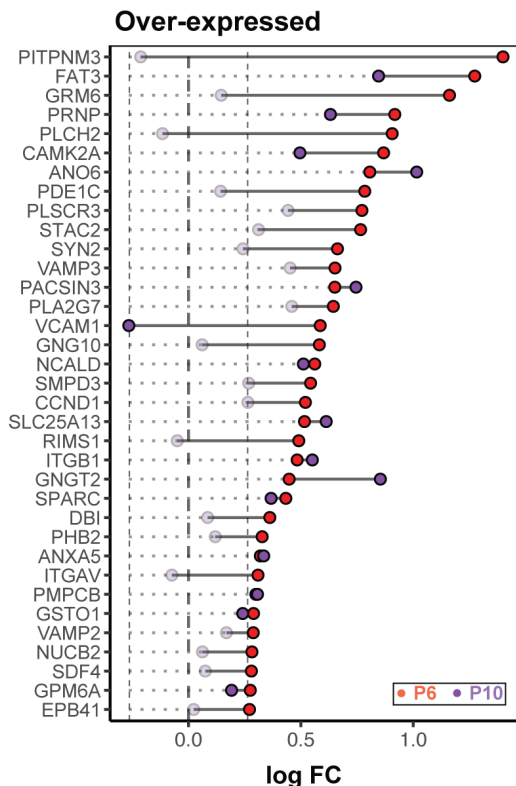


Figure 4

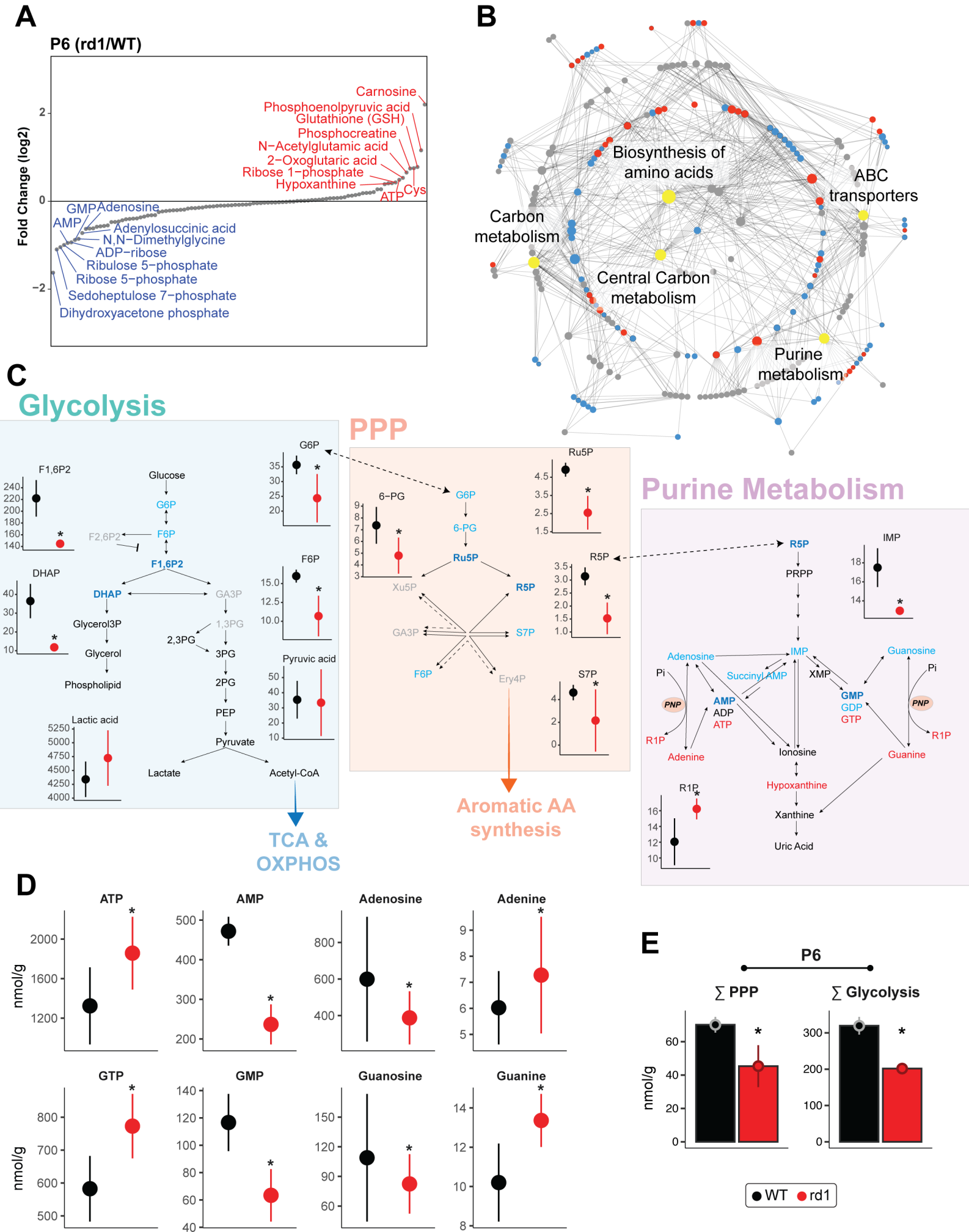
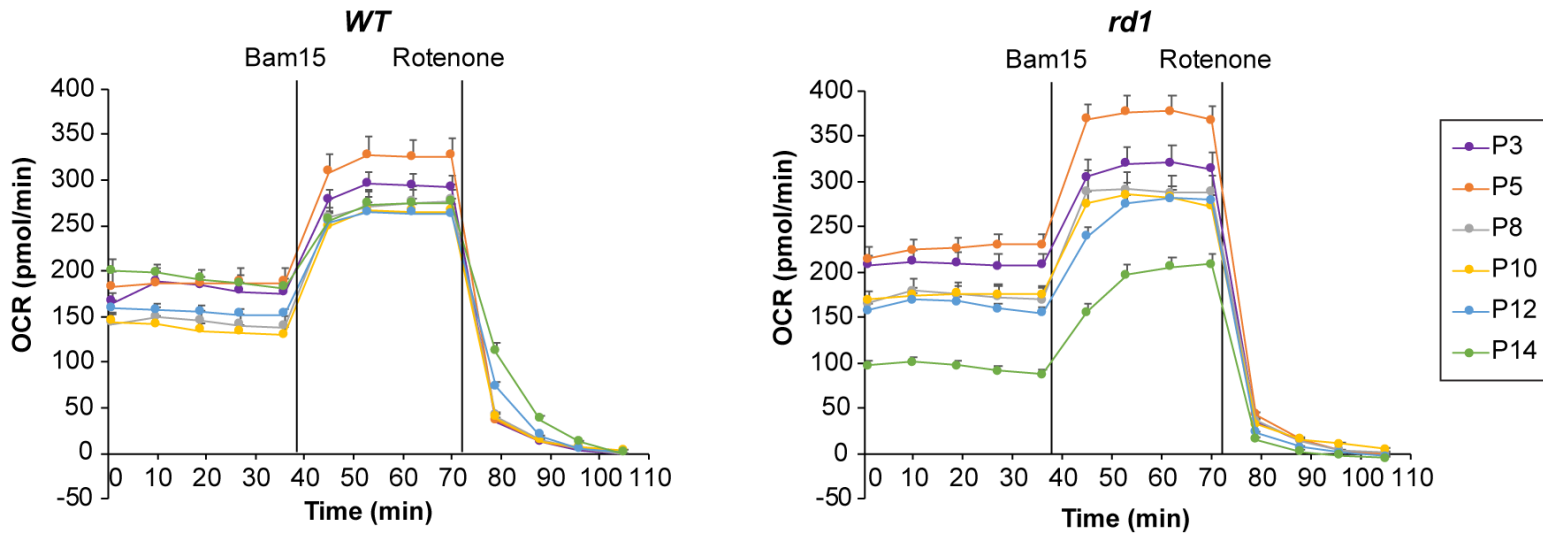


Figure 5

A



B

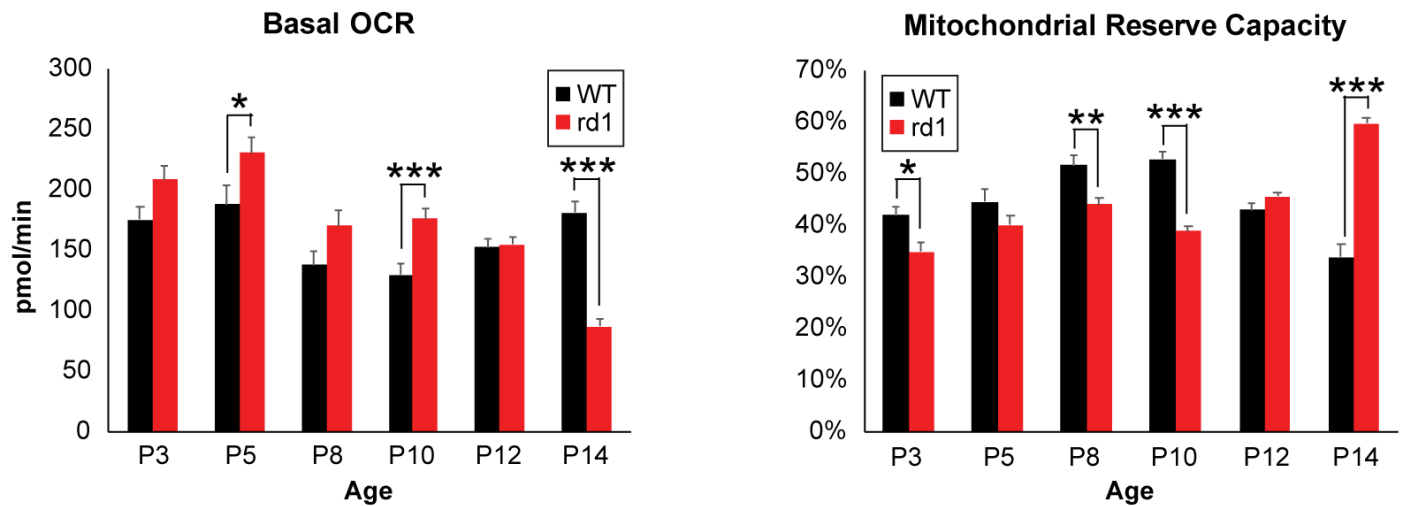


Figure 6

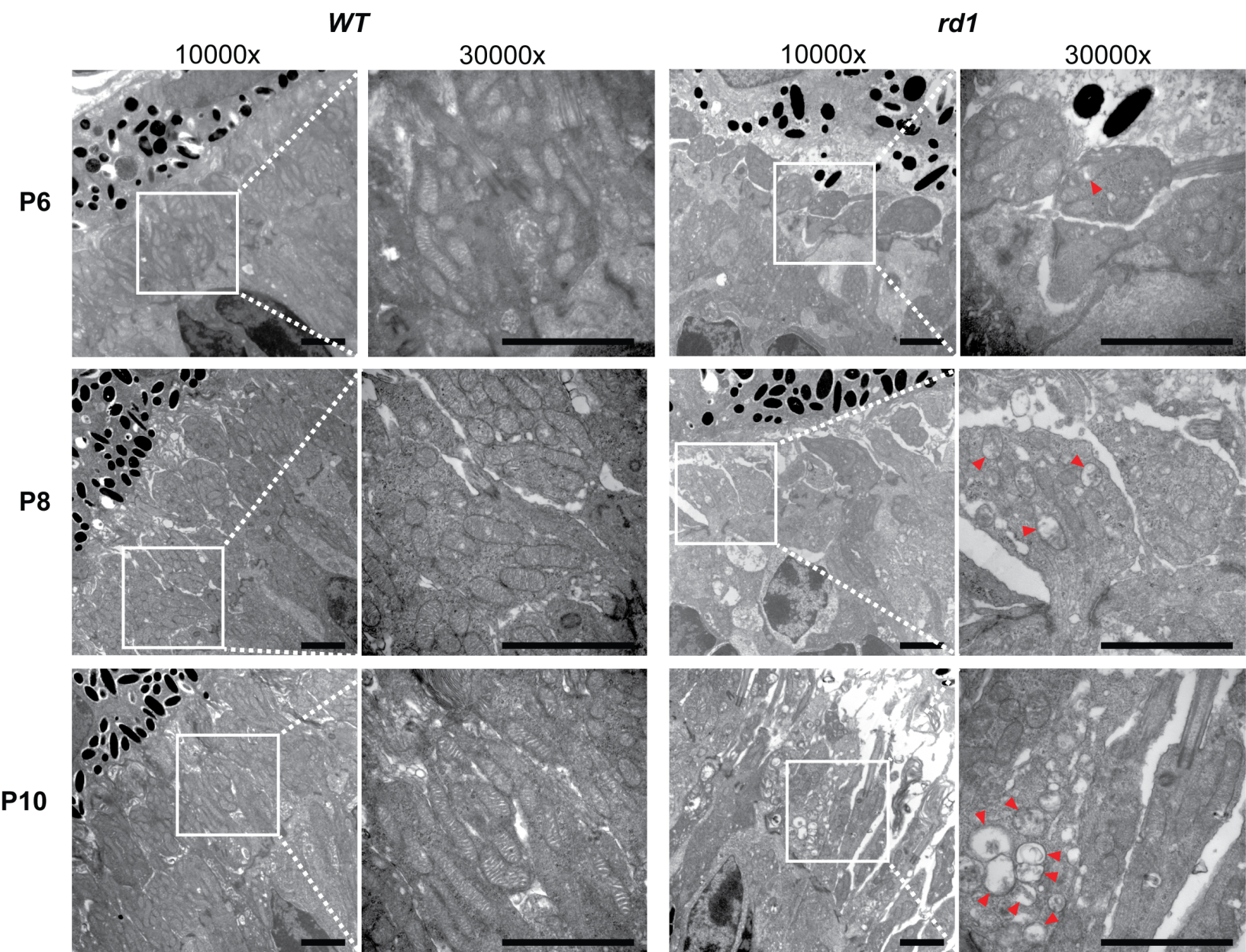


Figure 7

